# Modulations of the Indian summer monsoon by the hot subtropical deserts: Insights from coupled sensitivity experiments

**Sooraj K P[1], Pascal Terray[2,3], Sébastien Masson[2] and Julien Crétat[2]**

[1]Centre for Climate Change Research, Indian Institute of Tropical Meteorology, Pune 411008, India

[2]Sorbonne Universites (UPMC, Univ Paris 06)-CNRS-IRD-MNHN, LOCEAN Laboratory, 4 place Jussieu, Paris, France

[3]Indo-French cell for Water Sciences, IISc-IITM-NIO–IRD Joint International Laboratory, IITM, Pune 411008, India

Revised for climate dynamics

August 2018

---

Corresponding author address:

Sooraj K. P.

Centre for Climate Change Research, Indian Institute of Tropical Meteorology

Pune 411008, India, e-mail:sooraj@tropmet.res.in

**Abstract**

This study revisits the role of subtropical deserts in the Indian Summer Monsoon (ISM) system by perturbing surface albedo over the subtropical deserts, to the west of the ISM domain in different ways, using a state-of-the-art coupled model.

The analysis of up-to-date satellite datasets, atmospheric re-analyses and our control coupled simulation suggests that the model broadly reproduces the radiation budgets close to re-analyses and observed datasets. However, there are large uncertainties in the top-of-atmosphere radiation budget over the Northern Hemishere (NH) subtropical desert region during boreal summer; while the model has a rather neutral radiation budget during boreal summer over the Sahara Desert, the European Centre for Medium Range Weather Forecasts Interim reanalysis show in contrast a radiative excess throughout the NH desert region and the up-to-date satellite dataset has a clear negative radiation budget over north-eastern Sahara region and over Arabian Peninsula.

Taking into account these incertitudes, our key finding is that by darkening the deserts and arid regions to the west of ISM through a negative albedo perturbation in our coupled model, the length and intensity of the rainy season over the Indian region are both significantly increased with two well-defined rainfall anomaly maxima in May-June and September-October. The ISM onset is advanced by one month and is characterized by a rapid northward propagation of the rainfall band over the Indian domain.

Reversing the sign of our artificial albedo perturbation over the deserts in the model gives an opposite response, highlighting the robust role of the subtropical deserts in the ISM system, but the amplitude of the ISM response is also significantly larger, demonstrating nonlinearity in the monsoon-desert relationship. Additional albedo perturbation experiments further demonstrate

that the whole hot subtropical deserts extending across Afro-Asian continents, and including the Sahara, plays a key-role in the ISM response.

Finally, the modulations of the meridional tropospheric temperature gradient along with stronger equatorial asymmetry of mean easterly shear and moisture distribution over the Indian domain are key-factors for explaining the ISM response and its nonlinearity to the albedo perturbations over the NH subtropical deserts. Further insights from moisture budget show that the nonlinearity in advection moisture tendencies manifests in nonlinearity of the ISM response.

**Keywords:**

Indian summer monsoon; subtropical deserts; land albedo perturbations; radiation energy budget; monsoon seasonality; abrupt monsoon transition

## 1. Introduction

Monsoon and desert coexist as twins at the northern hemisphere (NH) subtropical latitudes of the African-Asian continent with their peak intensity during boreal summer (Rodwell and Hoskins 1996; Wu et al. 2009). Two important examples are the Arabian-Iran-Thar desert located just to the west of the Indian Summer Monsoon (ISM) system (Sikka 1997) and the Sahara just to the north of the West African Monsoon (WAM) system (Lavaysse et al. 2009). Consequently, relationships between monsoons and deserts have been widely investigated (Ramage 1966; Charney 1975; Webster 1994; Rodwell and Hoskins 1996; Bollasina and Nigam 2011a,b; Biasutti et al. 2009; Lavaysse et al. 2009; Bollasina and Ming 2013; Vinoj et al. 2014; Shekhar and Boos 2017; among many others).

The most conspicuous desert climate features include clear sky conditions, low rainfall, high temperature, reduced soil moisture, lack of vegetation and high surface albedo year around (Sikka 1997; Warner 2004). Radiative cooling of the atmospheric column prevails over these regions and is compensated by upper level atmospheric subsidence. On the other hand, intense solar heating of the surface during daytime and summer produces a strong SH flux into the lower atmosphere, which creates near-surface low pressure systems usually referred as “heat” lows (Ramage 1966; Warner 2004). The heat low over the Arabian-Iran-Thar desert is the deepest surface low-pressure system in the Tropics during boreal summer. Similarly, the Saharan Heat Low (SHL) over the Sahara is an important component of the WAM (Biasutti et al. 2009. Furthermore, these two regional heat lows are embedded within a gigantic subtropical heat trough across North Africa to West Asia during boreal summer. Here and after, we will refer collectively to these arid regions as the “hot subtropical desert”, which is broadly defined as the geographical region delimited by 20°W-75°E, 15°-40°N (as highlighted in Fig. 1a).

The traditional theory attributes the formation of subtropical deserts to the subsidence and associated adiabatic heating in the descending branch of the Hadley circulation (Warner 2004). This view is now recognized as imperfect (Yang et al. 1992; Rodwell and Hoskins 1996; Wang 2006; Wu et al. 2009) since the NH Hadley mean-circulation is the weakest during boreal summer when South Asia receives abundant monsoon rainfall and aridity is the highest to its west, over the hot subtropical desert, at about exactly the same latitudes.

Yang et al. (1992) and Webster (1994) have proposed the concept of a closed "Walker type" circulation linking convection, upward motion and diabatic heating over South Asia to subsidence over the hot subtropical desert in order to explain why these two climates coexist at the same time and latitude over the African-Asian continent. However, this view has been refuted by the seminal work of Rodwell and Hoskins (1996, 2001), which constitutes now the accepted paradigm for explaining the coexistence of the hot subtropical desert and ISM (Wang 2006; Bollasina and Nigam 2011a; Tyrlis et al. 2013; Cherchi et al. 2014).

In this theory, the aridity over the hot subtropical desert is still associated with the subsidence induced by ISM convective heating, but this subsidence is not explained by simple zonal-mean Hadley-cell or meridional-mean Walker-cell arguments (Lindzen and Hou 1988; Hoskins 1996; Rodwell and Hoskins 1996, 2001; Tyrlis et al. 2013; Cherchi et al. 2014). In particular, Rodwell and Hoskins (1996), demonstrated that remote diabatic heating over South Asia induces a Rossby wave pattern to its west and that the large-scale descent over the hot subtropical desert and the eastern Mediterranean region during boreal summer results mainly from the interaction between these westward propagating Rossby waves and the mid-latitude westerlies. Their trajectory analysis further revealed that the subsiding air over the hot subtropical desert is of mid-latitude origin. Subsequent studies showed additional contributions through local longwave radiative cooling (which they called a "local diabatic enhancement mechanism") in strengthening the descent over the hot subtropical desert (Rodwell and Hoskins 2001). This "monsoon-desert mechanism" further highlights that the hot subtropical desert is a rather "passive" recipient in the monsoon-desert relationship (Bollasina and Nigam 2011a).

From a different perspective, it is however generally agreed that the desert and arid regions play an important role on the WAM and ISM systems (Charney 1975; Charney et al. 1977; Shukla and Mintz 1982; Sud and Fennessy 1982; Sud et al. 1988; Claussen 1997; Bonfils et al. 2000; Douville et al. 2001; Xue et al. 2004; Yasunari et al. 2006; Xue et al. 2010; Bollasina and Nigam 2011b; Bollasina and Ming 2013). The relationship between variabilities of the WAM and SHL is for example well established (Haarsma et al. 2005; Biasutti et al. 2009; Lavaysse et al. 2009). ISM is also known to be associated with atmospheric variability over the arid regions to its west on a range of time scales (Ramage 1966; Smith 1986a,b; Mooley and Paolino 1988; Parthasarathy et al. 1992; Krishnamurti et al. 2010; Saeed et al. 2011; Bollasina and Nigam 2011b; Bollasina and Ming 2013; Vinoj et al. 2014; Rai et al. 2015). Bollasina and Ming (2013) found that surface heating over the northwestern semi-arid areas alone determines a realistic northwestward migration of the ISM at both the seasonal and intra-seasonal time scales without any external forcing (e.g. seasonal variations of insolation) in their Atmospheric General Circulation Model (AGCM). Vinoj et al. (2014), using also an AGCM, showed the short-term (within a week) modulation of ISM rainfall through the dust-induced land surface heating over North African and West Asian regions. Interestingly, these results coincided with a previous result that the boreal summer heat low over West Asian desert regions may serve as an important mechanism in controlling moisture transport into the ISM region (Smith 1986a,b; Mohalfi et al. 1998). More recently, Rai et al. (2015) and Chakraborty and Agrawal (2017) found a significant correlation between ISM variability and pre-monsoon atmospheric variations over the arid northwest India, Pakistan, Afghanistan and Iran regions. They argue that the heat low over these regions drives the monsoon winds during the first part of boreal summer.

Collectively, these studies demonstrate that the changes of surface heating over the hot subtropical desert can affect the ISM. Furthermore, they suggest that the heat lows are a key element in the monsoon circulations. However, this would seem to partly contradict the idea that the deserts and their associated heat lows are remotely forced by ISM through a Rossby wave response (Rodwell and Hoskins 1996, Bollasina and Nigam 2011a).

Here, we seek to resolve this paradox/contradiction in a coupled modeling framework by imposing different sets of surface land albedo over the hot subtropical desert to the west of the South Asian domain in an ocean-atmosphere coupled model. These experiments aim at providing new insights into the role of the arid regions in modulating the ISM rainfall and circulation.

Section 2 outlines the coupled ocean-atmosphere model, the design of our sensitivity experiments and the validation datasets used in this study. Section 3 reviews the radiation budget, both at the Top-Of-Atmosphere (TOA) and the surface, and the atmospheric circulation during boreal summer with a special focus on the hot subtropical desert and ISM, as seen in observations and our coupled model. Sections 4 and 5 describe the results of the sensitivity experiments. Section 6 provides a discussion on the specific role of the Sahara in the ISM response and addresses the robustness of our results with the help of another coupled model. Section 7 summarizes our main conclusions.

## 2. Coupled model, sensitivity experiments and validation datasets

Unless otherwise specified, our analysis and diagnostics mostly focus on the boreal spring-summer season from May to September.

## 2.a Climate coupled model

We used the SINTEX_F2 (SINTEX hereafter) coupled model for our control simulation and subsequent coupled sensitivity experiments. Refer to Masson et al. (2012) for a complete description of the version of the SINTEX model used here. The information regarding the atmospheric, oceanic and land components can be summarized as follows. The atmosphere model ECHAM5.3 is run at T106 spectral resolution, with 31 hybrid sigma-pressure levels (Roeckner et al. 2003). The oceanic component is the NEMO (Madec 2008) at 0.5° X 0.5° horizontal resolution, 31 vertical levels and with an interactive sea ice model. The atmosphere and ocean exchange quantities such as heat and momentum fluxes every 2 hours, with no flux adjustment or correction.

ECHAM5.3 uses a land surface scheme with prescribed white sky snow-free surface albedo climatology, but without any seasonal cycle (Roeckner et al. 2003). Following Terray et al. (2017), this old background albedo climatology has been updated by a seasonal varying snow-free background albedo climatology over land estimated from the Moderate Resolution Imaging Spectro-radiometer (MODIS) snow-free gap-filled white-sky (e.g. diffuse) albedo product MCD43GF-v5 over the 2003-2013 period (Schaaf et al. 2011). For more technical details on the original albedo parameterization in the ECHAM5.3 and on the updated version used here, readers are referred to Roeckner et al. (2003) and Terray et al. (2017), respectively. The tropical climate, including ISM, is better simulated by this updated SINTEX configuration (Terray et al. 2017).

2.b Coupled sensitivity experiments

Albedo, surface roughness and soil moisture play an important role in the simulation of the hot subtropical desert and its relationship with the adjacent monsoon systems as illustrated by numerous numerical studies focusing on the Holocene climate (Lofgren 1995; Bonfils et al. 2000) or the processes of desertification in the Sahel or South Asia regions (Charney 1975; Sud and Fennessy 1982; Laval and Picon 1986; Claussen 1997; Sud et al. 1998; Snyder 2010; Bollasina and Nigam 2011a,b; Pitman et al. 2011; Mahmood et al. 2014). These sensitivity studies typically increase (decrease) the surface albedo (or the surface roughness length) directly or indirectly (e.g. by changes in leaf area index and fractional green vegetation cover) in an atmospheric model. The findings suggest that such surface modifications over the arid regions alter the local climate and subsequently affect the adjacent monsoon systems through impacts on atmospheric dynamics and rainfall (Pielke 2001; Bollasina and Nigam 2011b; Agrawal and Chakraborty 2016). In a seminal paper, Charney (1975) suggested that desertification over the Sahel is a consequence of a positive feedback produced by the increased albedo associated with land degradation.

However, most of these previous modeling studies used stand-alone atmospheric or regional models, which may not be sufficient to account for all the feedbacks affecting the monsoon system. The climate sensitivity may be drastically modified because of the lack of ocean-atmosphere coupling and the fact that Sea Surface Temperatures (SST) are often specified as seasonally varying climatological values in these experiments. This is an important shortcoming, especially for the monsoon regions (Wang et al. 2004, 2005, 2008; Wu and Kirtman 2005; Kumar et al. 2005; Prodhomme et al. 2014, 2015).

Thus, our primary goal is to reinvestigate the remote impacts of changes in surface albedo over the hot subtropical desert on the ISM with the help of our updated SINTEX configuration. More precisely, we performed a total of 7 coupled experiments starting at the same initial conditions, but differing only in the specifications of the background surface (diffuse) albedo over the subtropical deserts (see Table 1).

First, a control simulation (referred throughout the manuscript as CTRL) of 110 years is performed with the updated SINTEX configuration. We then conducted a series of six coupled sensitivity experiments of 60 years each. In the first one (called here and after as Desert_Arab_m20), the background land albedo has been artificially decreased by -20% over the Arabian-Pakistan-Thar desert (15°-40°N, 35°-75°E as highlighted in Fig. 1d). A similar experiment, but with an artificial increase of +20% over the same domain, has also been performed (called here and after as Desert_Arab_p20). Third and fourth sensitivity experiments are similar, but the artificial decrease/increase of background albedo concerns the whole hot subtropical desert extending up to the Sahara in the west (called here and after as Desert_m20 and Desert_p20, respectively, See Fig. 1a and Table 1). Finally, in Section 6, we discussed the results of sensitivity experiments with albedo perturbations only over the Sahara desert (15°-40°N, 20°W-35°E as highlighted in Fig. 1b. See Table 1 for further details.

Differences between the simulated climate in each experiment and CTRL were computed (after removing the first ten years of the simulations), which we broadly refer to as “anomalous responses” or simply “responses” to albedo perturbations over selected desert regions. Note that using only the first 60 years in CTRL run or excluding 15 or 20 years from the various runs do not change the results, consistent with our earlier investigations that 50 years of simulation is sufficient to assess the response due to a given albedo perturbation (e.g. Terray et al. 2017).

A local statistical test is applied to the rainfall differences fields in order to assess the statistical significance of the results. The statistical significance of the differences was estimated through a permutation test with 9999 shuffles, and rainfall differences significant at the 95% confidence level are indicated in the figures. More details about this statistical test are given in Terray et al. (2003).

2.c Observed and reanalysis datasets

To validate model outputs, we make use of the following datasets: 1) monthly-accumulated precipitation from the Global Precipitation Climatology Project (GPCP version 2.1; Huffman et al. 2009) over the 1985-2014 period; 2) monthly-mean atmospheric variables (i.e. surface skin temperature (TS), three dimensional circulation and mean sea-level pressure (MSLP)) derived from the 2.5° ERA-Interim (ERAi) reanalysis produced by the European Centre for Medium-Range Weather Forecasts (http://apps.ecmwf.int/datasets/data/interim-full-daily; Dee et al. 2011), over the 1979-2014 period and 3) the Clouds and the Earth's Radiant Energy System Energy Balanced and Filled (CERES-EBAF edition 2.8; Kato et al. 2013) for TOA and surface from the period 2001–2015 is also used to validate the radiation fluxes from the model simulations and the ERAi reanalysis.

## 3. The monsoon-desert system in observations, reanalysis data sets and coupled control simulations

We first provide a validation of SINTEX in this section. Since many studies have already documented the mean and variability of ISM using SINTEX (e.g. Masson et al. 2012; Joseph et al. 2012; Terray et al. 2012, 2016, 2017; Prodhomme et al. 2014, 2015, Crétat et al. 2016), we focus on the Desert climate and its connections to ISM with the help of an energy budget analysis and a tridimensional atmospheric view of the monsoon-desert system.

As a starting point, we begin with the radiation and energy budgets at TOA and the surface over the desert region during boreal summer (Table 2). Note that the albedo values given in Table 2 are defined as the ratio between reflected and incoming shortwave radiations at the surface (or TOA), which differs from the prescribed background snow-free albedo in the model (as discussed in Section 2.a). First, the results comprehensively highlight many of the desert characteristics (Warner 2004), with the desert incurring large shortwave radiation loss (at both TOA and surface) due to high surface albedo and large long-wave upward emission from the surface due to the high surface temperature. Furthermore, the net long-wave radiation budget is highly deficient both at TOA and surface, consistent with the facts that the atmosphere over the desert is cloud-free with a reduced water vapor content (Neelin and Held 1987; Raymond 2000; Wang and Dickinson 2013).

A conspicuous feature is that the desert has a net gain of radiative energy both at the surface and TOA despite of the large upward long-wave emission during boreal summer, with net radiation estimates of around 90 $Wm^{-2}$ at the surface and between 16-30 $Wm^{-2}$ at TOA depending on the datasets. Note that earlier studies usually reckon the deserts to be large-scale radiative energy sinks on the annual mean time scale, with the Outgoing Long-wave Radiation (OLR) exceeding the net solar radiation at TOA (e.g. Charney 1975; Wang 2006). Accordingly, the TOA net radiative budget over the desert from ERAi turns out to be -8 $Wm^{-2}$, at the annual time scale. The corresponding annual estimates from CERES-EBAF and CTRL also show a radiative loss amounting to -19 and -10 $Wm^{-2}$, respectively. In contrast, during the boreal summer, Table 2 indicates that the net radiation budget estimates at TOA over desert show a radiative heating of about 30 $Wm^{-2}$ in ERAi and CTRL and 16 $Wm^{-2}$ in CERES-EBAF (see Table 2). A look at the spatial maps (Fig. S1) however suggests large uncertainties in the regional aspects of the TOA radiation budget over NH desert region during boreal summer. For example, the couple model has a rather neutral radiation budget over the Sahara Desert (Fig. S1c). But the reanalysis show a radiative excess throughout the NH desert region (Fig. S1b). Note that earlier observational studies (using NIMBUS-7 radiation budget, Smith 1986a,b) also showed surplus radiative energy over the Arabian desert which is again in contrast with the observed estimates from CERES-EBAF (Fig. S1a). As per the other studies, the boundary layer dust is observed to increase the short-wave absorption and this dust-induced heating overcomes the long-wave radiative deficit over the Arabian desert, thus producing either a radiative neutral or an energy surplus at TOA and strengthening of the heat low over there during boreal summer (Ackerman and Cox 1982; Mohalfi et al. 1998).

Focusing now on the energy balance at the surface, Table 2 shows that approximately 75% of the net radiation gain for the surface is partitioned to sensible heat flux (SH), while about 20% contributes to latent heat flux (LH) in ERAi. SINTEX reasonably captures this surface energy balance since the SH and LH represent, respectively, 85 and 10% of the available radiative energy at the surface in CTRL. However, as expected, the LH flux estimates differ significantly between ERAi and CTRL in absolute value, highlighting the large incertitude of this component of the energy budget, even for the desert region where evaporation is small and precipitation very sporadic (Wild et al. 2015).

It is also worth noting, finally, that the ERAi radiation estimates are more comparable to CTRL than CERES-EBAF. Consistently, recent studies noted that ERAi contains significant differences at the surface and TOA for radiative fluxes at the annual time scale, when compared to CERES-EBAF (Wild et al. 2015; Rai et al. 2017). This highlights the uncertainties in state-of-the-art atmospheric re-analyses. The radiation budget estimates specifically focusing on Afro-Asian subtropical deserts are not so much, except a few studies (e.g. Haywood et al 2005; Cherchi et al 2014; Blake et al 1983; Smith 1986a,b), which also showed the large errors in the estimation of net radiation flux at TOA. These studies attributed the discrepancies to uncertainties in the radiation parameterization code (e.g. absorption bands), which might also result from errors in surface temperature, surface albedo and dust aerosol effects.

We performed similar budget diagnostics over ISM land domain (Table 3). Firstly, the vegetated land surface over South Asia shows a much smaller surface albedo as compared to the surface of the desert, but TOA albedo is stronger in all datasets. Consistently, net shortwave radiation at the surface is much reduced by about 50 $Wm^{-2}$ compared to the desert estimates, highlighting the important role of clouds and a moist atmosphere. Secondly, the net long-wave losses both at the surface and TOA over these cloudy regions (Table 3) are less compared to that of arid regions, as the clouds and moisture tend to absorb the upward long-wave flux emitted from the ground (Raymond 2000; Neelin and Held 1987). Finally as expected, the LH fluxes largely dominates the SH fluxed over the ISM region.

We next looked at the seasonal evolution of monsoon rainfall over the Afro-Asian region with a special focus on ISM (Fig. 1). In April, the Inter-Tropical Convergence Zone (ITCZ) is located just south of the Equator over the Indian Ocean (IO) with two maxima, one off shore of Sumatra and the second off the African coast, while the ITCZ already straddles the Equator over the Atlantic Ocean (Fig. 1a). The commencement of rainy season in the IO occurs first over the Sumatra region with the northward expansion of rainfall over Bay of Bengal and eastern Arabian Sea in May (Fig. 1b). On the other hand, during this month, the northward migration of the ITCZ over the western IO and the African sector is very slow (e.g. about 1° of latitude). Afterwards, the monsoon convection spreads northwards leading to the ISM onset over the regions neighboring southern India during June (Fig. 1c). The monsoon penetrates further to central Indian landmass in the subsequent months while the ITCZ is located more southward and looks almost stationary in the African region (Fig. 1d-e).

CTRL shows a very similar rainfall evolution. The spatial correlations between CTRL and GPCP are always above 0.73 for the tropical domain (i.e. within 20°S to 35°N; see Fig. 1) from April to September. However, the simulated precipitation exhibits some well-known biases with a more southward position of the ITCZ in the African sector, excessive rainfall over the IO north of the equator and deficient rainfall over the eastern equatorial IO and the central Indian landmass (Joseph et al. 2012; Terray et al. 2012; Prodhomme et al. 2014).

To set the stage for further understanding on the monsoon-desert system, Figure 2 shows the vertical structure of vertical velocity and horizontal divergence, along a pressure-longitude plane averaged over 15°-30°N from May to September in ERAi and CTRL. The southern limit of the domain is set at 15°N since this is approximately the boundary between the rainy and desert regions in the Afro-Asian sector during boreal summer (Fig. 1).

As expected, ERAi shows centers of strong summertime ascent (see shading in Fig. 2) with a marked seasonal evolution in the east, contrasting with well-defined subsidence from 200 to about 600-hPa to its west, especially during May-June (see Fig. 2a-b). The strong ascent, extending throughout the troposphere, is situated over the Indian landmass and Bay of Bengal (Indo-BoB region, 70°-90°E) and reaches a maximum peak at July (Fig. 2a-c), thus, consistently following the seasonal evolution of ISM rainfall (Fig. 1). As a thermodynamic response to the vertical motion induced by diabatic heating (Neelin and Held 1987), there is low-level convergence (see contours in Fig. 2) with associated low-level westerlies (not shown), and upper-level divergence associated with upper-level easterlies (not shown) over the ISM domain, thus resembling a baroclinic structure during the whole boreal summer (Jiang et al. 2004).

In May, one can also detect several well defined regional heat lows showing convergence and ascending motion limited to lower levels (e.g. between the surface and 600-hPa) consistent with the dry convection affecting these arid regions. This near-surface upward motion is also quickly damped due to the counteracting effect of the prominent mid-to-upper level subsidence between TOA and about 700-hPa (Fig. 2a). However, two interesting points are (i) the notable abatement of this upper-level subsidence after May (Fig. 2b-c), coinciding with the northward shift of the monsoon activity over the Indo-BoB longitudes (Fig. 1c-e), and (ii) the persistence of the heat lows in July-August despite the surface temperature has significantly decreased at this time (figure not shown). Furthermore, there is a tendency for the regional heat lows to merge together from May to July leading to the formation of a gigantic heat trough after the sudden attenuation in the upper level subsidence (Fig. 2a-c). CTRL shows a similar evolution of the vertical velocity and convergence fields (Fig. 2f-j). The above description highlights the forcing of the hot subtropical desert by the South Asian monsoon (Rodwell and Hoskins 1996, 2001; Bollasina and Nigam 2011a), but, surprisingly, also a possible relaxation of this forcing after the ISM onset in both ERAi and CTRL.

We extended our analysis in Figure 2, by examining the seasonal evolution of vertical motion and horizontal divergence over 30°-40°N (Fig. 3). Upward motion can still be noticed eastward of 80°E over these latitudes, which correspond to the high Tibetan plateau, during the whole ISM period. Distinct and strong descent centers can also be distinguished: one over west Asia (in between 60°-70°E) and another one over the eastern Mediterranean region (in between

10°-40°E), with the later one fully consistent with the monsoon-desert paradigm (Rodwell and Hoskins 1996, 2001). In fact, the entire troposphere over the eastern Mediterranean sector is under a strong descent regime. Interestingly, the subsidence over this region intensifies from May to July (Fig. 3a-c and f-h), which is in contrast with what happened over the south part of the hot subtropical desert where subsidence decreases over the same time interval (Fig. 2a-c and f-h). The subsidence weakens only at a slow pace in August, with an accelerated weakening thereafter. This evolution over the northern part of the desert domain (e.g. 30°-40°N) is again well reproduced by CTRL (Fig. 3f-j).

In summary, the aforementioned features highlight the very different vertical structure of the atmospheric circulation over the southern and northern regions of the hot subtropical desert. They also qualify the coupled model for a reasonable representation of the monsoon-desert system over the Afro-Asian region, especially the vertical structure between northern and southern boundaries of the hot subtropical desert, the heat lows over the subtropical deserts as well as the vertical atmospheric structure associated with the ISM, which are the features believed to be important for further understanding of the relationships between ISM and the deserts in the next sections.

## 4. ISM response to reduced surface albedo over the hot subtropical desert

In this section, we focus on the responses resulting from an artificial decrease in surface albedo over the whole hot subtropical desert and the Arabia-Middle-East desert in the coupled model (e.g. the Desert_m20 and Desert_Arab_m20 experiments in Table 1).

### 4.1 Energy budget and ISM rainfall response

Table 4 shows the energy budgets at TOA and the surface over the hot subtropical desert in Desert_m20 and over the Arabia and Middle-East desert in Desert_Arab_m20, along with their differences from CTRL. First, the results comprehensively highlight the changes in radiative forcing caused by a surface albedo perturbation over the deserts. The surface albedo over the deserts decreases by -19 % in the two experiments, e.g. by about the same amount as imposed in the background land albedo in these experiments (see Table 1). As expected, the amount of shortwave radiation absorbed by the surface increases (by about +31 $Wm^{-2}$), but also at TOA (about +25 $Wm^{-2}$). This results in surface warming (of about 3K) and stronger surface upward long-wave emission (about -19 $Wm^{-2}$). However, this radiative loss subsequently gets offset by an even larger increase of downward long-wave flux, as indicated by the positive value of net long-wave radiation budget at the surface in Desert_m20 (e.g. +6 $Wm^{-2}$). This demonstrates the existence of a positive feedback amplifying the original surface warming due solely from the surface albedo perturbation. The LH and SH latent fluxes also increase, with the later one dominating over the other (-8 and -29 $Wm^{-2}$, respectively). However, both the LH and rainfall responses dominate the SH response in relative terms (the relative increases in LH and rainfall are 89% and 160%, respectively, while it is only 39% in SH flux), suggesting a significant increase of the water vapor content of the atmosphere over the hot subtropical desert in the experiments with a possible effect on the net long-wave radiation budget at the surface as described above.

The net radiation budget at TOA is even more positive than at surface in Desert_m20 (about +39 $Wm^{-2}$ at TOA compared to +37 $Wm^{-2}$ at the surface) leading to a modest radiative warming of the whole atmospheric column over the hot subtropical desert (about +2 $Wm^{-2}$). The Desert_Arab_m20 experiment leads to similar results over the Arabia and Middle-East desert

(Table 4). The basic inference here is that by perturbing the surface albedo over the subtropical deserts, we not only change their surface thermal characteristics, but also somewhat modify the whole tropospheric column above the hot subtropical deserts as we will further demonstrate below.

This excess of energy over the deserts leads to modifications of the energy budget over the ISM region and an increase of ISM rainfall in Desert_m20 or Desert_Arab_m20 (Table 5). Albedo over the ISM landmass remains unchanged at the surface, but increases at TOA in both experiments (3% and 2%, respectively). This suggests increased cloud cover and abundant moisture consistent with the enhanced rainfall in the two experiments (+2 and +1 mm/day in Desert_m20 and Desert_Arab_m20, respectively; corresponding to an increase of 34% and 16%, respectively). Accordingly, there is a modest decrease in net solar radiation both at TOA and surface over the ISM region (e.g. -13 $Wm^{-2}$ at TOA and -16 $Wm^{-2}$ at surface in Desert_m20 for example; see Table 5) in agreement with a cooling of the land surface (e.g. -0.7°C and -0.3°C in Desert_m20 and Desert_Arab_m20, respectively; see Table 5). This shortwave radiation loss, is only partly compensated by an increase of the net long-wave radiation (e.g. +9 $Wm^{-2}$ and +4 $Wm^{-2}$, respectively at TOA and surface in Desert_m20; see Table 5), again in agreement with a more cloudy and moist atmosphere over the Indian landmass in both Desert_m20 and Desert_Arab_m20. Finally, the enhanced ISM rainfall is associated with an increase of LH flux, but again the changes are more significant in Desert_m20 than Desert_Arab_m20.

Figures 4 (on the time-latitude evolution of monthly precipitation) and S2 (on the spatial evolution of rainfall response) further illustrate the significant differences in ISM responses between the two experiments. A notable feature in both the experiments is an early ISM onset with a spatially well-organized rainfall band between 5°-15°N occurring as soon as in May (see

Fig. 4b-c and Fig. S2b). The ITCZ, usually located over the equator during May, has already moved to the north, thus occupying the eastern Arabian Sea and then extending to BoB region in both the experiments (compare Figs. 1b and S2b). However, the Desert_m20 simulates a much faster northward rainfall migration and more intense precipitation anomalies, with two well-defined maxima in May-June and September-October, leading to a significant increase of the ISM length (Fig. 4b). In contrast, the rainfall anomalies in Desert_Arab_m20 quickly fade away after May-June (Fig. 4c). This suggests that some positive feedbacks are at work when we considered the whole hot subtropical desert in the experiments.

### 4.2 Tropospheric temperature and humidity responses

Consistent with previous studies, the early ISM onset in the experiments is tightly linked to the evolution of the tropospheric temperature over the Asian land mass, north of 20°N (shading in Fig. 5; e.g. Li and Yanai 1996; and He et al. 2003; Xavier et al. 2007; Prodhomme et al. 2015; Sabeerali and Ajayamohan 2017), and to the increase of the near surface humidity north of the Equator (contours in Fig. 5; Goswami 2005; Ramesh Kumar et al. 2009; Goswami et al. 2010; Chakraborty and Agarwal 2017).

Substantial enhanced warming is observed at low-levels between 25°-35°N corresponding to regions from northwest India extending toward Pakistan and part of Afghanistan suggesting that the artificial decrease of the albedo in the two experiments helps in enhancing the surface heat low over these regions during late spring and early summer. As a further proof of this assertion, Figure 6 displays the spatial patterns of TS, 850-hPa wind and MSLP anomalies during ISM in Desert_m20. As expected, the largest MSLP decreases occur mainly over the hot subtropical desert, where TS increases mostly due to the albedo perturbation introduced in Desert_m20 (Table 4). Interestingly, SST response over the IO in Desert_m20 is of very modest amplitude despite of the fact that MSLP anomalies extend well over the ocean (Fig. 6). This indicates that TS anomaly over land is the major driver of the extended MSLP trough and the associated low-level circulation, which develops during boreal summer in Desert_m20. Similar features, but of reduced amplitude and spatial extension, are seen in Desert_Arab_m20 (not shown).

Tropospheric warming is also observed at nearly all pressure levels northward of 20°N in the domain 55°-75°E in Desert_m20 during May-June, enhancing significantly the Meridional Tropospheric Temperature Gradient (MTTG) in the Indian sector (Fig. 5a-f). On the other hand, such changes in the upper atmosphere (above 500-hPa) are intriguingly much less pronounced in Desert_Arab_m20 with a significant tropospheric warming mostly restricted to atmospheric levels below 500-hPa (see Fig. 5g-l). These results from Desert_m20 suggest the key-role of the hot subtropical deserts extending across Afro-Asian continents in the tropospheric temperature and rainfall response over the Indian Sector. It also demonstrates that the regional differences in the mid and upper troposphere are key factors controlling the differences in ISM responses between Desert_m20 and Desert_Arab_m20 (Fig. 4b-c; see He et al. 2003; Dai et al. 2013).

In order to elucidate the origin of the tropospheric warming at higher levels during the onset and withdrawal phases of ISM in the two perturbation experiments, Figure 7 shows the anomalous 300-hPa wind and temperature responses in Desert_m20 and Desert_Arab_m20, during May, June and September. Well defined anticyclonic circulation and warm temperature anomalies are found at 300-hPa over the whole hot subtropical desert (the Arabia and Middle-East deserts) during May-June in Desert_m20 (Desert_Arab_m20) illustrating the strong baroclinicity of the atmospheric response (Figs. 7a-b and 7d-e; see Fig. 6 for the surface response in Desert_m20) to the albedo perturbations. This suggests first a local contribution from surface heating of the Sahara and Arabian deserts and the elevated regions of Iran, Afghanistan and Pakistan.

Despite these similarities, the overall 300-hPa temperature response in Desert_m20 is overwhelming compared to Desert_Arab_m20 during the ISM onset phase (see Figs. 7a-b and 7d-e). The most notable feature is the existence of a pronounced upper level warming (ranging from 1 to 1.5°C) between 20° to 35°N and extending far away eastward in Desert_m20. This suggests that the enhanced warming of the atmospheric column over the whole hot subtropical desert in Desert_m20 (see Table 4) may also be advected eastward by the climatological upper-level westerlies during April-June (figures not shown). These results are consistent with earlier studies arguing that the heat advection associated with the Sub-Tropical westerly Jet stream (STJ) and related planetary waves during April-June (Figure not shown) can influence the temperature of the landmass lying north of ISM region (Xavier et al. 2007). Similar anomalous features are observed during September in Desert_m20 (Fig. 7c). On the other hand, in Desert_Arab_m20, the upper troposphere shows only subtle warming response during the ISM onset and withdrawal phases (Figs. 7d,e and f).

The reasons for this upper-level differential warming between the two experiments are further explored in Figure 8, which shows latitudinal vertical cross-sections of monthly temperature (in shading) and vertical velocity (in contours) anomalies averaged over the North African longitudes 20°W-30°E. In April-May, the lower troposphere gets heated from below through the exchange of SH fluxes in Desert_m20 (Table 4) and this low-level warming expands vertically in the middle and upper atmosphere (Fig. 8a-b). By June, upper-level (e.g. above 300-

hPa) warming starts intensifying around 20°-30°N, coinciding with the appearance of wide spread upper-level subsidence northward of 25°N (Fig. 8c) which is manifested in adiabatic descent causing warming in the upper atmospheric column. Note that warming may also be due to the horizontal temperature advection as suggested by Cherchi et al. (2014) based on their study over the same domain. Thereafter, this upper-level warming gets slightly weakened in agreement with the disappearance of upper-level subsidence anomalies during July and August, but both the anomalies (i.e. upper-level warming and subsidence) are again enhanced in September. This remarkably concurs with the observed waning of enhanced ISM convection during July and August, but its revival during September-October in Desert_m20 (Fig. 4b and Fig. S2). In other words, this coupled pattern of upper-level warming and subsidence anomalies at subtropical latitudes of North Africa is consistent with the monsoon-desert paradigm of Rodwell and Hoskins (2001; see their Fig. 5) and is probably induced by the enhanced deep convection over ISM region during both the first and last parts of boreal summer in Desert_m20 (see Fig. 4b and Fig S2). During July-August (Fig. 8d-e), one can see the emergence of large-scale ascending motion and warming anomalies between 300 and 500-hPa from 15° to 30°N, which coincide with the strengthening of the WAM in Desert_m20 (Fig. S2d-e).

In contrast, the tropospheric warming over Africa is quite feeble in Desert_Arab_m20 (right panels of Fig. 8), where the surface albedo is not perturbed over the Sahara region and despite of the fact that ISM is also enhanced in this experiment. There appears to be only modest descent and warming around 20°-35°N at upper-levels throughout June to September, which probably coincides with the convection anomalies over ISM region (Rodwell and Hoskins 2001). The modulation of the WAM and the associated warming in the middle atmosphere is also fully missing here in contrast to Desert_m20. Finally, the differential response in the middle and upper troposphere over Africa between the two experiments, further suggests the significant role of the Sahara for sustaining the warming of the whole tropospheric column and the subsequent eastward warm advection at upper-levels at the subtropical latitudes in Desert_m20 (Fig. 7).

4.3 ISM circulation response

We now examine the ISM atmospheric circulation response in Desert_m20, which shows the larger ISM rainfall response.

In Desert_m20, the atmospheric wind anomalies observed in May (Fig. 9a) are reminiscent of the mean-conditions observed during June in CTRL (not shown). One can see a deep layer (between the surface and 600-hPa, Figs. 5b, 6a and 9a) of anomalous moist south-westerlies blowing across the Arabian Sea extending up to 15°N, instead of a shallow layer (between the surface and 800-hPa) of weak and drier low-level climatological westerlies extending only 10°N (figure not shown). Consistently, Desert_m20 shows also the early appearance of a pronounced Tropical Easterly Jet (TEJ, Wang 2006) in May, anomalously extending northward between Equator and 20°N, along with the anomalous northward displacement of STJ at upper-levels. The mean easterly shear is also enhanced north of the equator in May, thus paving the way for an early ISM onset (Goswami 2005; Xiang and Wang 2013; Prodhomme et al. 2015; Parker et al. 2016). In other words, all these features confirm that the stronger asymmetry of mean easterly shear and moisture distribution with respect to the equator may be key-factors for explaining the early and abrupt monsoon transition in Desert_m20 experiment (e.g. Webster and Yang 1992; Wang and Xie 1996; Xie and Wang 1996; Jiang et al. 2004).

This also highlights a strong association between the seasonal march of the whole ISM circulation and the heating over the hot subtropical desert since all the above described atmospheric anomalies, especially the strengthened TEJ and the enhanced vertical easterly shear observed between 10°-25°N, are consistent with the thermal wind relationship and the warming of the whole tropospheric column northward of 20°-25°N observed from May to June (Fig. 5b-c; e.g. Dai et al. 2013; Xavier et al. 2007; Ueda et al. 2006; Wu et al. 2012).

As a further confirmation of this tight thermal wind relationship for explaining the anomalous ISM circulation in Desert_m20, the upper-level easterly and vertical shear anomalies subsequently weaken during July-August (Fig. 9c-d) as the tropospheric warm anomalies northward of 25°N in Desert_m20 also show similar signature (Figs. 5c-d). Such damping of the atmospheric and rainfall anomalies during the peak phase of the monsoon in Desert_m20 may be related to the dominance of the convective processes for regulating the evolution of the MTTG and ISM circulation through latent heat release in the troposphere (Wang 2006; Xavier et al. 2007; Prodhomme et al. 2015) or to competitions between the WAM and ISM (see shading in Fig. S2). Finally, the revival of the ISM circulation and rainfall during September (Figs. 4b and 9e) is again associated with an enhanced tropospheric warming in the northern parts of the domain (Fig. 5f). This concomitant evolution of ISM rainfall and MTTG confirms again the relevance of the MTTG to measure the ISM strength in our experiments.

## 5. ISM response to increased surface albedo over the hot subtropical desert

Here, we address the robustness and possible nonlinear nature of the relationship between ISM and hot subtropical desert with the help of Desert_p20 and Desert_Arab_p20 experiments (see Table 1 for more details). For conciseness, we will illustrate the responses mostly by using

Desert_p20, as Desert_Arab_p20 shows similar features, though of modest amplitude, as already illustrated by Desert_Arab_m20 in Section 4.

5.1 Energy budget and ISM rainfall response

Despite of the fact that the amplitude of the artificial perturbations imposed in Desert_p20 and Desert_m20 is exactly the same, the response in the simulated albedo and net shortwave radiation budgets at the surface and TOA are stronger in Desert_p20 (Table 6) with a decrease in solar shortwave radiation absorption at the ground (about -46 $Wm^{-2}$) and at TOA (about -40 $Wm^{-2}$), as compared to those in Desert_m20 (+31 $Wm^{-2}$ and +25 $Wm^{-2}$, respectively at surface and TOA, see Table 4). As less radiative energy is available at surface, both the surface temperature and upward long-wave emission decrease substantially in Desert_p20, much more than the corresponding increase for Desert_m20 (see Tables 4 and 6). However, this reduced upward long-wave emission from the surface is fully compensated by a parallel decrease of the downward long-wave emission since the net long-wave radiation budgets at surface are almost similar in Desert_p20 and Desert_m20, with an excess of about 6 $Wm^{-2}$ compared to CTRL. As a consequence, the loss of shortwave radiation at the surface in Desert_p20 (e.g. -46 $Wm^{-2}$) is almost exclusively compensated by a large decrease of the SH flux (e.g. 38 $Wm^{-2}$) since the LH flux anomaly is very small (e.g. 2 $Wm^{-2}$). This highlights the key role of the SH flux anomalies over the Desert for explaining the differences in the amplitude of ISM response between Desert_p20 and Desert_m20. These asymmetrical results are similarly seen in the Desert_Arab_p20 experiment as well (e.g. Tables 4 and 6).

This asymmetric nature of the atmospheric response is also observed over ISM region as Table 7 shows decreased rainfall in the Desert_p20 (-3.2 mm $day^{-1}$) and Desert_Arab_p20 (-2.2

mm day$^{-1}$) experiments. Quantitatively, these rainfall responses in Desert_p20 and Desert_Arab_p20 represent, respectively, a decrease of 53% and 36%, while the corresponding increases are only of 34% and 16% in Desert_m20 and Desert_Arab_m20.

This decreased ISM rainfall in turn implies cloud-less conditions and less moisture, which is further manifested by an important decrease in TOA albedo over the Indian domain (-8%, see Table 7). Accordingly, there is stronger increase in net solar radiation both at TOA and surface over the ISM region (e.g. 37 Wm$^{-2}$ at TOA and 45 Wm$^{-2}$ at surface in Desert_p20 for example; see Table 7), with the net long-wave radiation partially offsetting it (e.g. -28 Wm$^{-2}$ at TOA and -13 Wm$^{-2}$ at surface in Desert_p20; see Table 7), which is further consistent with a strong surface warming (e.g. 2 and 1 K in Desert_p20 and Desert_Arab_p20, respectively; see Table 7). Finally, as expected, the LH (SH) flux decreases (increases) over the ISM region compared to CTRL since less moisture is available at the surface (see Table 7).

Figure 10 shows the seasonal evolution of rainfall response along 70°-90°E, from Desert_p20 and Desert_Arab_p20 experiments. The response from Desert_p20 includes a slower monsoon transition, a decrease in ISM rainfall during the whole boreal summer, which, in conjunction with a late ISM onset and an early ISM withdrawal, results in a pronounced shrinking of the length and intensity of the rainy season (Fig. 10a). Desert_Arab_p20 also shows a similar response, but with a less obvious modulation in the length of the rainy season (Fig. 10b).

Based upon the responses in energy budget and rainfall (compare Figure 4 and Table 4 with Figure 10 and Table 6), one can infer that the positive perturbation experiments (e.g. Desert_p20 and Desert_Arab_p20) consistently produce stronger responses than their negative counterparts during the whole boreal summer season. This illustrates the key importance of the fluctuation in the SH fluxes over the hot subtropical desert for the ISM rainfall and circulation as shown next.

## 5.2 Tropospheric temperature and humidity responses

Figure 11 shows the seasonal evolution (from April to September) of the tropospheric temperature and specific humidity responses from the Desert_p20 as latitude-pressure diagrams averaged between 55°-75°E. Substantial tropospheric cooling is observed northward of 20°N, which expands vertically in the middle and upper troposphere from April to June (Fig. 11a-c). During July and August, this tropospheric cooling decreases slightly, especially in the middle troposphere (e.g. between 600 and 400-hPa), but is again well pronounced in September (Fig. 11d-f). These tropospheric cooling pattern and evolution look symmetrically opposite to those noticed in Desert_m20 (e.g. Fig. 5, see section 4), implying a reduced MTTG over the region, especially at the start and end of ISM consistent with the ISM rainfall evolution in Desert_p20 (Fig. 10a). There is also a large reduction in meridional humidity gradient, which, in combination with tropospheric cooling, may stabilize the atmosphere and hence explains the rainfall suppression over the Arabian Sea and the Indian land mass during ISM.

We have also examined the seasonal evolution of temperature and vertical velocity anomalies as latitudinal vertical cross-sections averaged over the longitudes 20°W-30°E in Desert_p20 (figure not shown for brevity). In April-May, the lower troposphere (particularly north of 20°N) gets asymmetrically cold from the surface (Table 6), which expands vertically with time as in the Indian domain. Notably, the signature of cooling is prevalent throughout the column, but with no amplified cooling at the upper-level, even though the vertical motion shows anomalous tropospheric ascent north of 20°N. The implication is that the enhanced cooling, which is prevalent throughout the troposphere, is of local origin due to the imposed artificial surface albedo perturbation and the related enhanced SH flux anomaly over the deserts. This is further illustrated by Fig. 12, which displays the MSLP, TS and 850-hPa anomalous patterns in Desert_p20. A cold surface temperature anomaly coupled with an anomalous anticyclonic response persists at the surface of the hot subtropical desert during the whole ISM. Interestingly, as in Desert_m20 (Fig. 6), the SST response is only of small amplitude, even on the Arabian Sea.

Next we show the anomalous responses in 300-hPa wind and temperature for May, June and September from Desert_p20 (Fig. 13) when the MTTG is largely reduced over the Indian domain (e.g. Fig. 11b, c and f). Interestingly, at this level, one can find an anomalous cyclonic circulation over the hot subtropical desert during May-June and September. This is in contrast to the 300-hPa anomalous anticyclonic circulation over the same region in Desert_m20 (as noted in Section 4), highlighting again the strong baroclinicity of the atmospheric response to the surface albedo perturbations. Also, there is wide spread upper level cooling along the subtropical latitudes of the hot subtropical desert region, which is quite analogous to the pronounced upper level warming in Desert_m20. This may be again a signature of climatological upper-level westerly wind acting on the temperature anomalies, following the interpretation of the eastward temperature advection in Section 4.

On the other hand, the tropospheric cooling is much weaker over both Sahara and Indian regions in Desert_Arab_p20 experiment (figures not shown), which suggests again the possible role of the Sahara in explaining the differences between Desert_p20 and Desert_Arab_p20 (Table 6). The specific role of the Sahara in the experiments will be discussed in more details in Section 6.

## 5.3 ISM circulation response

For more detailed understanding on the underlying processes, we next examine the ISM circulation in Desert_p20 (Fig. 14). In Desert_p20, one can see dry low-level (between the surface and 800-hPa) easterly anomalies over the Arabian Sea in May (Figs. 11b, 12a and 14a), in contrast to deep anomalous moist westerly anomalies in Desert_m20 (Figs. 5b, 6a and 9a). These surface easterly anomalies in Desert_p20 are part of the anomalous surface anticyclone, which forms with the anomalous cyclonic circulation at higher levels (from 600 to 300-hPa), a robust baroclinic structure to the west of ISM region during the whole boreal summer (Figs. 12 and 13). This is further supported by tropospheric descent anomalies north of 20°N over the Indian landmass, which expand considerably to the south (up to 10-15°N) and vertically from May to June (not shown), thus impeding the ISM onset progression and hence leading to a delayed onset and weaker ISM in Desert_p20. Accordingly, the appearance of TEJ and northward migration of STJ at upper levels are conspicuously absent in Desert_p20 during May and June (Fig. 14a-b). These aforementioned features further confirm that the stronger MTTG along with the equatorial asymmetry of mean easterly shear and moisture are vital in determining the seasonal transition and maintenance of the ISM system.

## 5.4 Origin of the asymmetry in ISM rainfall responses between Desert_p20 and Desert_m20

A relevant question here is on the origin of the enhanced large-scale rainfall suppression and dryness over the Indian land mass longitudes in Desert_p20 (Fig. 10) compared to the ISM rainfall increase in Desert_m20 (Fig. 4).

Here we carried out additional diagnostics using a moisture budget analysis to discern the underlying moistening and drying process and to unravel the origin of non-linear anomalous responses between the two simulations (Desert_m20 and Desert_p20). The time mean budget moisture budget equation (e.g. Dixit et al. 2018) is as follow:

$$P = E - u\frac{\partial q}{\partial x} - v\frac{\partial q}{\partial y} - w\frac{\partial q}{\partial p} \qquad (1)$$

Here $P$ is rainfall and $E$ is evaporative latent heat flux over the ISM domain (see Tables 5 and 7). Also, $u, v \; and \; w$ are zonal, meridional and vertical pressure velocity, with $q$ being specific humidity. The equation can be applied to the control (CTRL) and perturbed (e.g. Desert_m20 and Desert_p20) simulations to get the anomalous responses (against CTRL).

Figure 15 shows the vertical profile of anomalous moisture advection tendencies for the two experiments (Desert_m20, left panels and Desert_p20, right panels). In Desert_m20 (Fig 15a-e, see the shading), the anomalous moistening due to vertical advection tendency prevails throughout the middle troposphere during the early and late parts of ISM and is in phase with the seasonal rainfall evolution depicted in Figure 4b, and hence dominantly contributes to the anomalous rainfall evolution. Horizontal anomalous advection in Desert_m20 (contours in Figure 15a-e) moistens the lower boundary layer due to the early penetration of monsoon flow to Indian latitudes in the Arabian Sea (see Fig 6a) and thus also contributes to the rainfall anomalies, but only during the first phase of ISM in Desert_m20. It seems that the horizontal advection also moistens the lower-troposphere to the northward edge of the rainfall peak, thus paving the way for the seasonal migration of rainfall and hence the abrupt monsoon transition in Desert_m20.

In Desert_p20 (Fig 15f-j), the budget responses are of amplified magnitude throughout the season relative to Desert_m20 and for both the vertical and horizontal moist advection terms, thus highlighting the non-linear nature of the anomalous dynamical response. This results in a pronounced and non-linear tropospheric drying effect and the consequent large-scale rainfall suppression over the Indian continent as described above (e.g. Section 5.2 and Fig. 10).

In other words, the asymmetric responses in ISM circulation and rainfall between Desert_p20 and Desert_m20, as discussed in Section 5.2, are tightly associated with the non-linearity in advection moisture tendencies. This further points towards some important positive feedbacks between the moisture convergence and the ascending motion (figure not shown) in the atmospheric column over land, which are much more active in Desert_p20, thus contributing to the large-scale suppression of rainfall over Indian continent in this simulation (as depicted in Fig. 10).

For explaining these differences one can further envisage the enhanced responses in TS and MSLP in Desert_p20 (see Table 6 and Fig. 12b-e) as compared to Desert_m20 (Table 4 and Fig. 6b-e), which thus contribute to the differences between Desert_p20 and Desert_m20 through geostrophic low-level wind adjustments and related anomalous moisture convergence at the low-levels during ISM (Figs. 6 and 12; see also Samson et al. 2016; Terray et al. 2017).

In a similar manner, the decrease of the LH flux over the Indian landmass in Desert_p20 (e.g. 24 $Wm^{-2}$; see Table 7) is stronger in amplitude than its increase in Desert_m20 (e.g. -10 $Wm^{-2}$; see Table 5). This reduced evaporation over land can again reduce the local moisture availability and, thus, contributes to further reduce the local diabatic heating of the atmospheric column and feedbacks on itself, leading to a stronger ISM response in Desert_p20. This stronger local effect in Desert_p20 may also reflect the tendency of the ground over India to become more easily saturated in Desert_m20, thus limiting the local LH flux and diabatic heating anomalies in this simulation. Recently, Halder et al. (2016) and Paul et al. (2016), using sensitivity experiments with regional climate models, similarly showed that the decrease in local moisture can efficiently reduce the low-level moist static energy, thereby increasing the atmospheric stability and suppressing the large-scale convective instability as well as convective activity.

It should be reminded, however, that in our simulations the activation of these positive feedbacks, involving local evaporation, moisture convergence and diabatic heating over India, is ultimately linked to the remote radiative forcing induced by the surface positive albedo perturbation over the hot subtropical desert to the west of the Indian domain in Desert_p20.

## 6. Discussion

6.a Specific role of the Sahara in the ISM circulation and rainfall responses

In earlier sections, we infer that the inclusion of the Sahara made a significant difference in radiative forcing, but also in the ISM rainfall and circulation responses based on the comparison of our Desert and Desert_Arab simulations. While these results suggest the potential significance of the Sahara, these simulations are not sufficient to delineate properly the specific role of the Sahara in the ISM response because the magnitude of radiative forcing in both simulations is hugely different and the response is probably nonlinear as highlighted in the previous sections.

In order to bring out the relative importance of Sahara and the Arabian-Pakistan-Thar deserts for ISM, we carried out additional perturbation runs only over the Sahara region (e.g. with artificial changes of -0.2 and 0.2 in the background land albedo over the Sahara region; see Table 1 and Fig. 1b for details).

The ISM rainfall response in these experiments, which we refer as Desert_Sahara_m20 and Desert_Sahara_p20, is displayed in Fig. 16. The results show a significant response with stronger (weaker) amplitude for a negative (positive) albedo perturbation as compared to those from Desert_Arab_m20 (Desert_Arab_p20) experiments (Figs. 4c, 10b). This demonstrates first the specific role of the Sahara warming/cooling on the ISM. The response is concentrated during the onset and first phases of the ISM, thus indicating a short-lived influence with no significant modulation in the length of the ISM rainy season as in the Desert_Arab experiments.

Again, the amplitude of the ISM response is stronger with a positive albedo perturbation (Fig. 16b), further highlighting the nonlinearity of the governing processes. Furthermore, the response to the forcing of the whole NH subtropical desert (i.e. ISM response from Desert_m20 and Desert_p20 experiments; see Figs. 4b, 10a) is significantly stronger than the addition of those responses due to the Sahara (Figs. 16) and Arabia-Middle-East (Figs. 4c and 10b) deserts separately, thus further attesting to the non-linearity of the relationship between the NH subtropical deserts and ISM.

### 6.b Robustness of the results

Our aforementioned model results however need obviously some cautionary remarks, because they can be model dependent. Furthermore, the specific coupled model SST biases may also affect the realism of the findings. Thus, the robustness of these results/conclusions needs to be verified with other coupled/forced models, especially the asymmetric ISM response. Hence in this direction, we have performed the same experiments with another coupled model, the CFSv2 model, currently in use at NCEP and IITM for seasonal forecasting (see Saha et al. 2014 and Terray et al. 2017 for details). Importantly, CFSv2 includes completely different atmospheric, oceanic and land dynamic components than SINTEX. Another interesting point is that both CFSv2 and SINTEX share exactly similar rainfall biases, however their SST biases are nearly opposite in most of the tropical regions (Terray et al. 2017). More specifically, CFS has a cold SST bias over the Indian Ocean (Swapna et al. 2015), while SINTEX has a warm bias over the Indian Ocean (Joseph et al 2012).

Figure S3 shows the ISM rainfall seasonal cycle in the control simulation and the responses in various experiments performed with CFSv2. A comparison of Figs. 4, 10 and S3 shows that the ISM rainfall responses are qualitatively and quantitatively very similar in the two models despite their important differences in parameterizations or SST bias. More specifically, there is an abrupt and early ISM onset transition in the CFSv2 Desert_m20 experiment, with a significant increase of ISM length (Fig. S3b). Figure S4 then highlights the strong association between the seasonal march of the ISM circulation and heating over the hot subtropical desert with associated increase of the inter-hemispheric MSLP gradient over western part of Indian domain, which is further instrumental in enhanced cross-equatorial flow and moisture convergence to the Indian landmass. The circulation and heating patterns in CFSv2 are very similar to those obtained with SINTEX (see Fig. 6).

Again consistent with SINTEX, qualitatively opposite rainfall response and associated heating patterns, but of asymmetric nature (e.g. stronger), are produced in Desert_p20 (Figs. S3c and S5), with an anomalous coupled pattern of cold surface temperature and anticyclonic circulation lying over the hot subtropical desert. Furthermore, the Desert_Arab_m20 and Desert_Arab_p20 experiments confirm the short-lived ISM response (compare Figs. 4c, 10b and S3d-e), indicating again the prominent role of the hot subtropical desert extending across the Afro-Asian continent on the ISM response. In other words, the nonlinearity of the ISM response is also found in the CFSv2 experiments.

## 7. Conclusion and Perspectives

During boreal summer, the South Asian monsoon and subtropical deserts coexist at the same latitudes over the African-Asian continent. Previous studies have tried to explain this coexistence, as well as the mutual relationships between these two very different climates (Yang et al. 1992; Webster 1994; Rodwell and Hoskins 1996, 2001; Wu et al. 2009; Bollasina and Nigam 2011a; Tyrlis et al. 2013; Cherchi et al. 2014; Krishnamurti et al. 2010).

However, the significant relationship between monsoon rainfall biases and surface temperature, albedo and humidity biases over the adjacent subtropical deserts in current state-of-the-art climate models (Samson et al. 2016; Agrawal and Chakraborty 2016; Terray et al. 2017) warrants further investigations on the possible role of the NH subtropical deserts on ISM intensity and evolution. Moreover, desert amplification over the NH subtropical deserts during boreal summer is one of the main modes of surface temperature warming associated with anthropogenic climate change (Zhou 2016; Wei et al. 2017).

These considerations motivate our re-examination of the ISM-desert paradigm. In order to unravel new facets on the role of the hot subtropical desert on ISM, the present study uses a global ocean-atmosphere coupled model and a set of carefully designed experiments by perturbing surface albedo in different ways over the hot subtropical desert (or parts of it) to the west of the South Asian domain.

The analysis of up-to-date satellite datasets, atmospheric re-analyses and our control coupled simulation suggests that the model broadly reproduces the radiation budgets as seen in re-analyses and observed datasets. However there are large uncertainties in the surface and TOA radiation budgets over the NH subtropical desert region (Fig S1), with the budget estimates showing inconsistency regionally. While the budget estimates from reanalysis (ERAi) show a radiative excess (despite of large upward long wave emission) throughout the NH desert region during boreal summer, in contrast, our model estimates have rather neutral radiation budget over the Sahara Desert. A few early studies (Smith 1986a,b; Vinoj et al. 2014) already suggested that the hot subtropical desert (e.g. over Arabian Peninsula) do not show the radiative sink property during boreal summer which is again in contrast with the observed estimates from CERES-EBAF (Fig. S1a).

Our desert albedo perturbation experiments further confirm that variations of the surface radiation budget over the Desert or parts of it, may impact the boreal summer monsoon far away since ISM evolution and intensity are affected with opposite polarity to prescribed negative and positive albedo perturbations over the whole hot subtropical desert or part of it (e.g. the Arabia and Middle-East or Sahara deserts). Interestingly, the Sahara is also playing a significant role in the strength of this ISM response and not only the Arabian-Iran-Thar desert adjacent to the ISM domain, as demonstrated by the comparison of our Desert, Desert_Arab and Desert_Sahara simulations (Figs 4, 10 and 16).

A second (expected) finding is that by darkening the surface of the deserts and arid regions to the west of the South Asian domain, radiative heating of the surface is increased. Interestingly, this additional heating is not solely due to the surface's albedo direct effect on solar absorption, but also to an increase of the net long-wave radiation budget. This suggests the existence of a positive feedback amplifying the original surface warming due solely from the surface albedo perturbation. The modest absolute changes of latent heating and rainfall over the deserts in the reduced albedo experiments seem to be sufficient to amplify this original surface warming by an even larger increase of the downward long-wave emission received at the surface. This leads ultimately to more excess in the surface and TOA net radiation budgets over the deserts (e.g. Table 4).

This heating over the desert is communicated to the overlying atmosphere mainly by additional SH flux and dry convection due to the very low ambient soil moisture. It generates a well-defined baroclinic atmospheric response with cyclonic wind and negative MSLP anomalies near the surface (e.g. Fig. 6), and anticyclonic wind anomalies aloft in the middle and upper troposphere (Fig. 7). Such tropospheric heating and atmospheric responses affect the adjacent monsoon systems, including ISM, in several co-operating ways.

First, it is found that the tropospheric warming over the hot subtropical desert results also in warmer upper and middle troposphere over the northern latitudes of the Indian subcontinent due to warm advection by the STJ in the upper troposphere during the onset and withdrawal phases of ISM (Figs. 5-8). This leads to an increased MTTG over the South Asian domain, which favors a strengthening of the easterly vertical wind shear (e.g. in agreement with thermal wind balance; Fig. 9) during the first and last phases of ISM, in addition to the baroclinic atmospheric structure directly linked to the albedo perturbation described above.

Second, the enhanced surface heat low over the Arabian Peninsula and the Iran-Pakistan-Thar desert (due to the local surface warming) increases significantly the inter-hemispheric MSLP gradient over the western part of the Indian domain because this MSLP gradient is mainly controlled by the seasonal evolution of the MSLP fields over the land (Fig. 6; Li and Yanai, 1996). This generates an enhanced cross-equatorial flow along the African coast, which gradually becomes westerly over the Arabian Sea due to the Coriolis effect, enhancing the moisture convergence over the Indian landmass during boreal summer (Samson et al. 2016; Terray et al. 2017).

All these factors (e.g. the easterly vertical shear of the zonal wind and the additional moisture north of the equator) contribute to explain why the length of the ISM is substantially increased in our Desert_m20 simulation (Fig. 4b), by both an early onset and a late withdrawal of the monsoon. Thus, our reduced albedo experiments further validate the well-known results that a stronger MTTG along with stronger equatorial asymmetry of mean easterly vertical shear and moisture distribution, are key-factors for explaining the early and abrupt ISM onset (e.g. Goswami et al. 2010; Parker et al. 2016).

It must be noted, however, that this increase of the length of the rainy season is much stronger in Desert_m20 than in Desert_Arab_m20 (Fig. 4b-c), highlighting the key-role of the whole hot subtropical Afro-Asian desert in the response. The short-lived ISM response in Desert_Arab_m20 corroborates previous studies, which show a significant association between the modulations of the heat low spread across the northwest India, Pakistan, Afghanistan and Iran regions during the pre-monsoon period with the ISM intensity in its initial period, but with the land-atmosphere coupling losing its signature once the monsoon matures (Ramage 1966; Mooley and Paolino 1988; Rai et al. 2015; Agrawal and Chakraborty 2016).

Qualitatively opposite results are obtained with positive albedo perturbations (e.g. the Desert_p20 and Desert_Arab_p20 simulations). But, both the amplitude of the SH flux anomalies over the deserts (Tables 4 and 6) and of the ISM response (Figs. 4 and 10) are significantly stronger, highlighting non-linear characteristics of this response. In the positive albedo perturbations runs, there is a larger reduction of the MTTG and the meridional humidity gradient during the whole ISM season. Furthermore, the asymmetric responses in ISM circulation and rainfall between Desert_p20 and Desert_m20 are tightly associated with the non-linearity in advection moisture tendencies, as revealed through the application of moisture budget analysis (see Section 5.2; Fig. 15). This points toward some important positive feedbacks between the moisture convergence and the ascending motion in the atmospheric column over land (Halder et al. 2016; Paul et al. 2016), which are much more active in this simulation than in Desert_m20 despite of the fact that the amplitude of the imposed albedo perturbation is the same in these simulations.

We also demonstrate the robustness of the land-surface heating over subtropical deserts to the seasonal march of ISM by performing similar experiments with another independent coupled model (see Section 6b). The results validate all our conclusions about the significant and differential roles of the NH subtropical deserts, including the Sahara, on the ISM system since they are independent of parameterization schemes used in the coupled models or SST biases affecting the coupled models.

Finally, the robustness of the relationship between the ISM and the neighboring deserts to its west found here suggests that these driest regions may play an increasingly significant role in the ISM evolution in the future climate through the modulation of their intense surface warming.

**Acknowledgements**

This work is funded by the Earth System Science Organization, Ministry of Earth Sciences, Government of India under Monsoon Mission (Project No. MM/SERP/CNRS/2013/INT-10/002 Contribution #MM/PASCAL/RP/07). We sincerely thank Prof. Ravi Nanjundiah, Director, Indian Institute of Tropical Meteorology (IITM, India) and Dr R Krishnan, executive Director, Centre for Climate Change Research (at IITM, India) for all the support during the research study. This work is performed using the HPC resources from GENCI-IDRIS in France (Grants 2015, 2016, 2017 – 016895) and from Indian Institute of Tropical Meteorology in India. The CCCR, IITM is fully funded by the Ministry of Earth Sciences, Government of India.

## References


Ackerman SA, Cox SK (1982) The Saudi Arabian heat low: Aerosol distribution and thermodynamic structure. J Geophys Res 87:8991–9002.

Agrawal S, Chakraborty A (2016) Role of surface hydrology in determining the seasonal cycle of Indian summer monsoon in a general circulation model. Hydrol Earth Sys Sci Discuss 1–33.

Biasutti M, Sobel AH, Camargo SJ (2009) The role of the Sahara low in summertime Sahel rainfall variability and change in the CMIP3 models. J Climate 22:5755–5771. doi:10.1175/2009JCLI2969.1.

Blake DW, Krishnamurti TN, Low-Nam SV, Fein JS (1983) Heat low over the Saudi Arabian Desert during May 1979 (Summer MONEX). Mon Wea Rev 111:1759–1775

Bollasina M, Ming Y (2013) The role of land-surface processes in modulating the Indian monsoon annual cycle. Clim Dyn 41(9–10):2497–2509. doi:10.1007/s00382-012-1634-3

Bollasina M, Nigam S (2011a) The summertime "heat" low over Pakistan/northwestern India: evolution and origin. Clim Dyn 37:957–970

Bollasina M, Nigam S (2011b) Modeling of regional hydroclimate change over the Indian subcontinent: impact of the expanding Thar desert. J Climate 24: 3089–3106

Bonfils C, N de Noblet-Ducoudré, Braconnot P, Joussaume S (2000) Hot desert albedo and climate change: Mid-Holocene monsoon in North Africa. J Climate 14:3724–3737.

Chakraborty A, Agrawal S (2017) Role of west Asian surface pressure in summer monsoon onset over central India. Environ Res Lett 12

Charney JG (1975) Dynamics of deserts and drought in Sahel. Quart J Roy Meteor Soc 101: 193-202.

Charney J, Quirk WJ, Chow S, Kornfield J (1977) A comparative study of the effects of albedo change on drought in semi-arid regions. J Atmos Sci 34:1366–1385.

Cherchi A, Annamalai H, Masina S, Navarra A (2014) South Asian summer monsoon and eastern Mediterranean climate: the monsoon-desert mechanism in CMIP5 simulations. J Climate 27:6877–6903. doi:10.1175/JCLI-D-13-00530.1

Claussen M (1997) Modeling biogeophysical feedback in the Africa and India monsoon region. Clim Dyn 13:247–257.

Crétat J, Terray P, Masson S, Sooraj KP, Roxy MK (2016) Indian Ocean and Indian summer monsoon: relationships without ENSO in ocean-atmosphere coupled simulations. Clim Dyn doi:10.1007/s00382-016-3387-x

Dai et al (2013) The relative roles of upper and lower tropospheric thermal contrasts and tropical influences in driving Asian summer monsoons. J Geophys Res Atmos 118:7024–7045.

Dee DP et al. (2011) The ERA-Interim reanalysis: Configuration 683 and performance of the data assimilation system. Quart J Roy Meteorol Soc 137:553–597.

Dixit V, Sherwood S, Geoffroy O, Mantsis D (2018) The Role of Nonlinear Drying above the Boundary Layer in the Mid-Holocene African Monsoon. J Climate 31: 233–249.

Douville H, Chauvin F, Broqua H (2001) Influence of soil moisture on the Asian and African monsoons. Part I: Mean monsoon and daily precipitation. J Climate 14: 2381–2403

Goswami B N (2005) South Asian monsoon, in Intraseasonal Variability of the Atmosphere-Ocean Climate System, edited by W. K. M. Lau and D. E. Waliser, chap. 2, pp. 19–61, Springer-Praxis, Chichester, U. K

Goswami BN, Kulkarni JR, Mujumdar VR, Chattopadhyay R (2010) On factors responsible for recent secular trend in the onset phase of monsoon intraseasonal oscillations. Int J Clim 30(14): 2240–2246.

Haarsma R J, Selten FM, Weber SL, Kliphuis M (2005) Sahel rainfall variability and response to greenhouse warming. Geophys Res Lett 32:L17702

Halder S, Saha SK, Dirmeyer PA, Chase TN, Goswami BN (2016) Investigating the impact of land-use land-cover change on Indian summer monsoon daily rainfall and temperature during 1951-2005 using a regional climate model. Hydrol Earth Syst Sci 20(5):1765-1784

Haywood et al (2005) Can desert explain the outgoing longwave radiation anomaly over the Sahara during July 2013? J Geophys Res Atmos 110:4551–4563

He H, Sui CH, Jian M, Wen Z, Lan G (2003) The evolution of tropospheric temperature field and its relationship with the onset of Asian summer monsoon. J Meteorol Soc Jpn 81:1201–1223

Hoskins BJ (1996) On the existence and strength of the summer subtropical anticyclones. Bull Amer Meteor Soc 77:1287–1291.

Huffman GJ, Adler RF, Bolvin DT, Gu G (2009) Improving the global precipitation record: GPCP Version 2.1. Geophy Res Lett 36:L17808. doi:10.1029/2009GL040000

Jiang XN, Li T, Wang B (2004) Structures and mechanisms of the northward propagating boreal summer intraseasonal oscillation. J Climate 17:1022-1039.

Joseph S, Sahai AK, Goswami BN, Terray P, Masson S, Luo JJ (2012) Possible role of warm SST bias in the simulation of boreal summer monsoon in SINTEX-F2 coupled model. Clim Dyn 38:1561–1576

Kato S et al. (2013) Surface Irradiances Consistent with CERES-Derived Top-of-Atmosphere Shortwave and Longwave Irradiances. J Climate 26:2719–2740.

Krishnamurti TN, Thomas A, Simon A, Kumar V (2010) Desert air incursions, an overlooked aspect, for the dry spells of the Indian summer monsoon. J Atmos Sci 67:3423–3441.

Kumar KK, Hoerling M, Rajagopalan B (2005) Advancing dynamical prediction of Indian monsoon rainfall. Geophys Res Lett 32: L08704. doi:10.1029/2004GL021979.

Laval K, Picon L (1986) Effect of a change of the surface albedo of the Sahel on climate. J Atmos Sci 43:2418–2429.

Lavaysse C, Flamant C, Janicot S, Parker DJ, Lafore JP, Sultan B, Pelon J (2009) Seasonal evolution of the West African heat low: a climatological perspective. Clim Dyn 33:313–330

Li C, Yanai M (1996) The onset and interannual variability of the Asian summer monsoon in relation to land-sea thermal contrast. J Climate 9:358-375

Lindzen RS, Hou AY (1988) Hadley circulations for zonally averaged heating centered off the equator. J Atmos Sci 45:2416–2427

Lofgren BM (1995) Sensitivity of land-ocean circulations, precipitation, and soil moisture to perturbed land surface albedo. J Climate 8:2521–2542

Madec G (2008) NEMO ocean engine. Note du Pole de modelisation, Institut Pierre-Simon Laplace (IPSL) 27:1288-1619

Mahmood R et al (2014) Land cover changes and their biogeophysical effects on climate. Int J Climatol 34:929–953

Masson S, Terray P, Madec G, Luo JJ, Yamagata T, Takahashi K (2012) Impact of intra-daily SST variability on ENSO characteristics in a coupled model. Clim Dyn 39:681-707

Mohalfi S, Bedi HS, Krishnamurti TN, Cocke SD (1998) Impact of shortwave radiative effects of dust aerosols on the summer season heat low over Saudi Arabia. Mon Wea Rev 126: 3153–3168

Mooley DA, Paolino DA (1988) A predictive monsoon signal in the surface level thermal fields over India. Mon Wea Rev 116:256–264

Neelin J D, Held IM (1987) Modeling tropical convergence based on the moist static energy budget. Mon Wea Rev 115:3–12

Parker DJ, Willetts P, Birch C, Turner AG, Marsham JH, Taylor CM, Kolusu S, Martin GM (2016) The interaction of moist convection and mid-level dry air in the advance of the onset of the Indian monsoon. Quart J Roy Meteorol Soc 142:2256–2272.

Parthasarathy B, Rupakumar K, Munot AA (1992) Surface pressure and summer monsoon rainfall over India. Adv Atmos Sci 9:359–366

Paul S et al. (2016) Weakening of Indian summer monsoon rainfall due to changes in land use land cover. Sci Rep 6:32177

Pielke RA (2001) Influence of the spatial distribution of vegetation and soils on the prediction of cumulus convective rainfall. Rev Geophys 39:151-177.

Pitman AJ, Avila FB, Abramowitz G, Wang YP, Phipps SJ, de Noblet-Ducoudré N (2011) Importance of background climate in determining impact of land-cover change on regional climate. Nat Clim Change 1:472–475

Prodhomme C et al (2014) Impacts of Indian Ocean SST biases on the Indian Monsoon: as simulated in a global coupled model. Clim Dyn 42:271–290.

Prodhomme C et al (2015) Oceanic factors controlling the Indian summer monsoon onset in a coupled model. Clim Dyn 44:977–1002.

Rai A, Saha SK (2017) Evaluation of energy fluxes in the NCEP climate forecast system version 2.0 (CFSv2). Clim Dyn. doi:10.1007/s00382-017-3587-z

Rai A, Saha SK, Pokhrel S, Sujith K, Halder S (2015) Influence of pre-onset land-atmospheric conditions on the Indian summer monsoon rainfall variability. J Geophys Res Atmos 120:4551–4563

Ramage CS (1966) J Atmos Sci 23:144

Ramesh Kumar MR, Sankar S, Reason C (2009) An investigation into the conditions leading to monsoon onset over Kerala. Theoret Appl Climatol 95:69–82.

Raymond DJ (2000) Thermodynamic control of tropical rainfall. Quart J Roy Meteor Soc 126: 889-898

Rodwell MJ, Hoskins BJ (1996) Monsoons and the dynamics of deserts. Quart J Roy Meteorol Soc 122:1385–1404

Rodwell MJ, Hoskins BJ (2001) Subtropical anticyclones and summer monsoons. J Climate 14:3192–3211

Roeckner E et al (2003) The atmospheric general circulation model ECHAM5: Part 1: model description. Max-Planck-Institut fur Meteorologie, Hamburg, MPI-Report 349.

Sabeerali CT, Ajayamohan RS (2017) On the shortening of Indian summer monsoon season in a warming scenario. Clim Dyn. doi:10.1007/s00382-017-3709-7

Saeed S, Müller W, Hagemann S, Jacob D (2011) Circumglobal wave train and the summer monsoon over northwestern India and Pakistan: the explicit role of the surface heat low. Clim Dyn 37:1045–1060.

Saha S *et al.* (2014) The NCEP climate forecast system version 2. J. Climate **27**:2185–2208.

Samson G, Masson S, Durand F, Terray P, Berthet S, Jullien S (2016) Role of land surface albedo and horizontal resolution on the Indian Summer Monsoon biases in a coupled ocean-atmosphere tropical-channel model. Clim Dyn doi:10.1007/s00382-016-3161-0

Schaaf CB, Liu J, Gao F, Strahler AH (2011) Land Remote Sensing and Global Environmental Change. Remote Sens Glob Environ Chang 11:549–561

Shekhar R, Boos WR (2017) Weakening and Shifting of the Saharan Heat Low Circulation During Wet Years of the West African Monsoon. J Climate 30:7399-7422

Shukla J, Mintz Y (1982) Influence of land-surface evaporation on Earth's climate. Science 215:1498–1501

Sikka D R (1997) Desert climate and its dynamics. Curr Sci 72:35–46.

Smith EA (1986a) The structure of the Arabian heat low. Part I: surface energy budget. Mon Wea Rev 114:1067–1083.

Smith EA (1986b) The structure of the Arabian heat low. Part II: bulk tropospheric heat budget and implications. Mon Wea Rev 114:1084–1102

Snyder PK (2010) The influence of tropical deforestation on the Northern Hemisphere climate by atmospheric teleconnections. Earth Interact. 14:1–34

Sud YC, Fennessy M (1982) A study of the influence of surface albedo on July circulation in semi-arid regions using the GLAS GCM. Int J Climatol 2:105–125.

Sud YC, Shukla J, Mintz Y (1988) Influence of land surface roughness on atmospheric circulation and precipitation: A sensitivity study with a general circulation model. J Appl Meteor 27:1036–1054.

Swapna et al. (2015) The IITM earth system model. Bull Amer Meteor Soc 96:1351–1367. doi:10.1175/BAMS-D-13-00276.1

Terray P, Delecluse P, Labattu S, Terray L (2003) Sea Surface Temperature Associations with the Late Indian Summer Monsoon. Clim Dyn 21:593–618

Terray P, Kamala K, Masson S, Madec G, Sahai AK, Luo JJ (2012) The role of the intra-daily SST variability in the Indian monsoon variability and monsoon-ENSO–IOD relationships in a global coupled model. Clim Dyn 39:729–754

Terray P, Masson S, Prodhomme C, Roxy MK, Sooraj KP (2016) Impacts of Indian and Atlantic oceans on ENSO in a comprehensive modeling framework. Clim Dyn 46:2507–2533

Terray P, Sooraj KP, Masson S, Krishna RPM, Samson G, Prajeesh AG (2017) Towards a realistic simulation of boreal summer tropical rainfall climatology in state-of the-art climate coupled models. Clim Dyn doi:10.1007/s00382-017-3812-9

Tyrlis E, Lelieveld J, Steil B (2013) The summer circulation over the eastern Mediterranean and the Middle East: Influenceof the South Asian monsoon. Clim Dyn 40:1103–1123. doi:10.1007/s00382-012-1528-4.

Ueda H, Iwai A, Kuwako K, Hori ME (2006) Impact of anthropogenic forcing on the Asian summer monsoon as simulated by eight GCMs. Geophys Res Lett 33:L06703.

Vinoj et al. (2014) Short term modulation of Indian summer monsoon rainfall by West Asian dust. Nature Geo Science doi:10.1038/NGEO2017

Wang B (2006) The Asian Monsoon. Springer, Chichester.

Wang B, Xie X (1996) Low-frequency equatorial waves in vertically sheared zonal flow. Part I: stable waves. J Atmos Sci 53:449–467.

Wang B, Kang I, Lee J (2004) Ensemble simulations of Asian–Australian monsoon variability by 11 AGCMs. J Climate 17:803–818

Wang B, Ding QH, Fu XH, Kang I-S, Jin K, Shukla J, Doblas-Reyes F (2005) Fundamental challenge in simulation and prediction of summer monsoon rainfall. Geophys Res Lett 32:L15711

Wang B, Lee JY, Kang IS, Shukla J, Kug JS, Kumar A, Schemm J, Luo JJ, Yamagata T, Park CK (2008) How accurately do coupled climate models predict the leading modes of Asian-Australian monsoon interannual variability? Clim Dyn 30:605–619. doi: 10.1007/s00382-007-0310-5

Wang KC, Dickinson RE (2013) Global atmospheric downward longwave radiation at the surface from ground-based observations, satellite retrievals, and reanalyses. Rev Geophys 51:150–185

Warner TT (2004) Desert Meteorology Cambridge University Press, London, p 612

Webster PJ (1994) The role of hydrological processes in ocean atmosphere interactions. Rev Geophys 32(4):427–476

Webster PJ, Yang S (1992) Monsoon and ENSO: selectively interactive systems. Quart J Roy Meteor Soc 118:877–926

Wei N, Zhou L, Dai Y, Xia G, Hua W (2017) Observational Evidence for Desert Amplification Using Multiple Satellite Datasets Sci Rep 2043. doi:10.1038/s41598-017-02064-w

Wild M et al. (2015) The energy balance over land and oceans: an assessment based on direct observations and CMIP5 climate models. Clim Dyn 44:3393–3429.

Wu G, Liu Y, He B et al (2012) Thermal controls on the Asian summer monsoon. Sci Rep 2:1–7. doi:10.1038/srep00404

Wu GX et al (2009) Multi-scale forcing and the formation of subtropical desert and monsoon. Ann Geophys 27:3631–3644. doi:10.5194/angeo-27-3631-2009

Wu R, Kirtman BP (2005) Roles of Indian and Pacific Ocean air-sea coupling in tropical atmospheric variability. Clim Dyn 25:155–170

Xavier PK, Marzin C, Goswami BN (2007) An objective definition of the Indian summer monsoon season and a new perspective on the ENSO–monsoon relationship. Quart J Roy Meteor Soc 133:749–764

Xiang B, Wang B (2013) Mechanisms for the advanced Asian summer monsoon onset since the Mid-to-Late 1990s. J Climate 26:1993–2009.

Xie X, Wang B (1996) Low-frequency equatorial waves in vertically sheared zonal flows. Part II: unstable waves. J Atmos Sci 53:3589–3605

Xue Y, Juang HMH, Li WP, Prince S, Defries R, Jiao Y, Vasic R (2004) Role of land surface processes in monsoon development: East Asia and West Africa. J Geophys Res (Atmos) 109:03105–03128

Xue Y et al (2010) Global and temporal characteristics of seasonal climate/vegetation biophysical process (VBP) interactions. J Climate 23:1411–1433

Yang S, Webster PJ, Dong M (1992) Longitudinal heating gradient: another possible factor influencing the intensity of the Asian summer monsoon circulation. Adv Atmos Sci 9:397-410

Yasunari T, Saito K, Takata K (2006) Relative roles of large-scale orography and land surface processes in the global hydroclimate, Part I: Impacts on monsoon systems and the Tropics. J Hydrometeor 7:626–641.

Zhou L (2016) Desert amplification in a warming climate. Sci Rep 6. doi:10.1038/srep31065

**Figure captions:**

**Figure 1:** Spatio-temporal evolution of rainfall climatology (mm $day^{-1}$) for May to September. The overlying contours represent rainfall estimates from GPCP, while shading is the same from CTRL (control simulation). The contours are drawn following the shading convention and the 5 mm $day^{-1}$ contour is highlighted in thick black colour. The pattern correlation between CTRL and GPCP for the tropical domain (i.e. within 20°S to 35°N) is indicated in each panel. The boxed area in (a), (b) and (d) represent the hot subtropical deserts regions where artificial albedo perturbation experiments are carried out (see Table 1 for more details).

**Figure 2:** Seasonal evolution (May to September) of vertical component of velocity (shading, units in $10^{-2}$ Pa $s^{-1}$) and horizontal divergence (contours, units in $10^{-6}s^{-1}$), along a pressure-longitude plane averaged over 15°-30°N for ERAi (left panel, a-e) and CTRL (right panel, f-j). The negative (dashed) and positive (continuous) contours correspond, respectively, to absolute magnitudes of **1, 2, 3 and 4** units. The zero contours are highlighted in thick black colour.

**Figure 3 (a-j):** Same Figure 2, but for the vertical component of velocity (shading, units in $10^{-2}$ Pa $s^{-1}$) and horizontal divergence (contours, units in $10^{-6}$ $s^{-1}$), averaged over 30°-40°N. The negative (dashed) and positive (continuous) contours correspond, respectively, to absolute magnitudes of 1, 2, 3 and 4 units. The zero contours are highlighted in thick black colour.

**Figure 4:** (a) Time-latitude evolution of rainfall climatology (mm $day^{-1}$, containing both land and oceanic points) averaged along 70°-90°E, from CTRL. (b) and (c) time-latitude evolution of anomalous rainfall response (computed against the CTRL rainfall climatology, see Section 2) averaged along 70°-90°E from Desert_m20 and from Desert_Arab_m20, respectively. In (b) and (c), the responses that are above the 95% confidence level according to a permutation procedure with 9999 shuffles are encircled.

**Figure 5:** (Left Panel, a-f) Seasonal evolution (April to September) of response in temperature (shading, °C) and specific humidity (contours, x$10^{-3}$ Kg $Kg^{-1}$) along a pressure-latitude plane over the longitudes 55°-75°E, for Desert_m20 experiment. Right panel (g-l), same as (a-f), but for Desert_Arab_m20 experiment. The anomalous responses are computed against the CTRL climatology (see Section 2). The negative (dashed) and positive (continuous) contours correspond, respectively, to absolute magnitudes of 0.25, 0.5, 1, 1.5, 2, 2.5 and 3 units. The zero contours are highlighted in thick black colour.

**Figure 6:** Seasonal evolution (May to September) of response in MSLP (contours, hPa), TS (shading, °C) and 850-hPa wind ($ms^{-1}$) from Desert_m20 experiment. Negative (dashed) and positive (continuous) contours correspond respectively to magnitudes of 0.5, 1.5, 3, 4 and 6 units. The zero contours are not drawn. The anomalous response is computed against the CTRL climatology (see Section 2). Wind vectors of magnitudes exceeding 1 $ms^{-1}$ are only drawn.

**Figure 7**: Map of the anomalous responses in wind and temperature at 300-hPa for (a) May, (b) June and (c) September, from Desert_m20 experiments. (d)-(f), same as (a)-(c), but from Desert_Arab_m20. The anomalous response is against the CTRL climatology (see Section 2).

**Figure 8:** (Left Panel, a-f) Seasonal evolution (April to September) of response in temperature (shading, °C) and vertical component of velocity (contours, units is $10^{-2}$ Pa $s^{-1}$) along a pressure-latitude plane averaged over the longitudes 20°W-30°E, for Desert_m20 experiment. Right panel (g-l), same as (a-f), but for Desert_Arab_m20 experiment. The anomalous response is computed against the CTRL climatology (see Section 2). The negative (dashed) and positive (continuous) contours correspond respectively to magnitudes of 0.25, 0.5, 1, 2, 3, 4 and 5 units. The zero contours are highlighted in thick black colour.

**Figure 9: S**easonal evolution (May to September) of response in horizontal component of wind (zonal wind in shading and meridional wind in contours, $ms^{-1}$) along a pressure-latitude plane averaged over the longitudes 55°-75°E, for Desert_m20 experiment. The anomalous response is computed against the CTRL climatology (see Section 2). The negative (dashed) and positive (continuous) contours correspond respectively to magnitudes of 0.5, 1, 1.5, 2, 2.5 and 3 units. The zero contours are highlighted in thick black colour.

**Figure 10:** Time-latitude evolution of rainfall response (mm $day^{-1}$, averaged along 70°-90°E from the sensitivity experiments. In (a) from Desert_p20 and in (b) from Desert_Arab_p20. The anomalous responses are computed against the CTRL climatology (see Section 2). In all panels, the responses that are above the 95% confidence level according to a permutation procedure with 9999 shuffles are encircled.

**Figure 11:** Seasonal evolution (April to September) of response in temperature (shading, °C) and specific humidity (contours, $x10^{-3}$ Kg $Kg^{-1}$) along a pressure-latitude plane over the longitudes 55°-75°E, for Desert_p20 experiment. The anomalous response is computed against the CTRL climatology (see Section 2). The negative (dashed) and positive (continuous) contours correspond, respectively, to magnitudes of 0.25, 0.5, 1, 1.5, 2, 2.5 and 3 units. The zero contours are highlighted in thick black colour.

**Figure 12:** Seasonal evolution (May to September) of response in MSLP (contours, hPa), TS (shading, °C) and 850-hPa wind ($ms^{-1}$) from Desert_p20 experiment. Negative (dashed) and positive (continuous) contours correspond respectively to magnitudes of 0.5, 1.5, 3, 4 and 6 units. The zero contours are not drawn. The anomalous response is computed against the CTRL climatology (see Section 2). Wind vectors of magnitudes exceeding 1 $ms^{-1}$ are only drawn.

**Figure 13:** (a) Anomalous response in wind (ms$^{-1}$) and temperature (°C, shading) at 300-hPa, during May from Desert_p20 experiment. (b) and (c), same as (a), but for June and September, respectively. The anomalous response is computed against the CTRL climatology (see Section 2).

**Figure 14: S**easonal evolution (May to September) of response in horizontal component of wind (zonal wind in shading and meridional wind in contours, ms$^{-1}$) along a pressure-latitude plane averaged over the longitudes 55°-75°E, for Desert_p20 experiment. The anomalous response is computed against the CTRL climatology (see Section 2). The negative (dashed) and positive (continuous) contours correspond, respectively, to magnitudes of 0.5, 1, 1.5, 2, 2.5 and 3 units. The zero contours are highlighted in thick black colour.

**Figure 15:** (Left Panel, a-e) Seasonal evolution (May to September) of response in vertical moisture advection (shading, units is $10^{-3}$ Kg Kg$^{-1}$ day$^{-1}$) and horizontal moisture advection (contours, x$10^{-3}$ Kg Kg$^{-1}$ day$^{-1}$) along a pressure-latitude plane over the longitudes 75°-90°E, for Desert_m20 experiment. Right panel (f-j), same as (a-e), but for Desert_p20 experiment. The anomalous response is computed against the CTRL climatology (see Section 2). The negative (dashed) and positive (continuous) contours correspond respectively to magnitudes of 0.1, 0.2, 0.3, 0.4, 0.5 and 0.6 units. The zero contours are highlighted in thick black colour.

**Figure 16:** (a) Time-latitude evolution of rainfall response (mm day$^{-1}$, averaged along 70°-90°E from the Desert_Sahara_m20 experiment. In (b), same as (a) but for Desert_Sahara_p20 experiment. The anomalous responses are computed against the CTRL climatology (see Section 2). In (a) and (b), the responses that are above the 95% confidence level according to a permutation procedure with 9999 shuffles are encircled.

**Figure captions (Supplementary Figures):**

**Figure S1:** Climatological map of net radiation budget at TOA ($Wm^{-2}$, see Table 2 and Section 2 for more details on radiation budget) for June to September period. In (a). CERES-EBAF, (b) ERAi and (c) CTRL

**Figure S2:** Spatio-temporal evolution of rainfall (May to September, mm $day^{-1}$) response from the Desert_m20 experiment (in shading). The overlying contours are the rainfall response from Desert_Arab_m20. Negative (dashed) and positive (continuous) contours are drawn following the shading convention. The anomalous responses are computed against the CTRL climatology (see Section 2).

**Figure S3:** In (a) to (c), same as that of Figure 4, but for the various experiments (CTRL, Desert_m20 and Desert_p20), conducted using CFSv2 coupled model (see Terray et al. 2017). Similarly, in (d) and (e), same as that of Figure 11, but for Desert_Arab_m20 and Desert_Arab_p20 simulations, using CFSv2. The length of integration (i.e. using CFSv2) in CTRL simulation is for 40 years, while it is 20 years for the Desert_m20 and Desert_p20. Note that the configuration used for the experiments also takes advantage of up-to-date satellite MODIS data for estimating the background snow-free albedo as described in Terray et al. (2017). The first 10 years of all the simulations are excluded for all the analyses presented in the text. In (b) and (c), the responses that are above the 95% confidence level according to a permutation procedure with 9999 shuffles are encircled.

**Figure S4**: Seasonal evolution (May to September) of response in MSLP (contours, hPa), TS (shading, °C) and 850-hPa wind ($ms^{-1}$) from Desert_m20 experiment done using CFSv2 model. Negative (dashed) and positive (continuous) contours correspond respectively to magnitudes of 0.5, 1.5, 3, 4 and 6 units. The anomalous response is computed against the CTRL climatology.

Wind vectors of magnitudes exceeding 1 $ms^{-1}$ are only drawn. For more details of the CFS runs, please refer to the legend of Fig. S3.

**Figure S5:** Seasonal evolution (May to September) of response in MSLP (contours, hPa), TS (shading, °C) and 850-hPa wind ($ms^{-1}$) from Desert_p20 experiment done using CFSv2 model. Negative (dashed) and positive (continuous) contours correspond respectively to magnitudes of 0.5, 1.5, 3, 4 and 6 units. The anomalous response is computed against the CTRL climatology. Wind vectors of magnitudes exceeding 1 $ms^{-1}$ are only drawn. For more details of the CFS runs, please refer to the legend of Fig. S3.

**Table captions:**

**Table 1:** Details of coupled model experiments as performed using SINTEX-F2 coupled model. The first 10 years of all the simulations are excluded for all the analyses presented in the text. See Section 2 for more details of the experiments.

**Table 2:** The radiative and turbulent fluxes, at surface (SURF) and top of the atmosphere (TOA), averaged over the land points in the domain 15°-40°N and 20°W-75°E (e.g. hot subtropical desert region) for June to September (JJAS) season. Here, SW and LW are shortwave and long-wave radiations, respectively. Net Rad means net radiation following the formulation in Su and Neelin (2002). SH and LH are sensible and latent heat fluxes. TS and PR stands for surface skin temperature and rainfall, respectively. Fluxes are signed in the direction of the fluxes (i.e. negative sign indicates upward fluxes and vice-versa). Asterisk (*) in the Table represents that the rainfall (PR) is averaged using the GPCP data and not using ERAi estimates. All fluxes have energy units (Wm$^{-2}$) and albedo is in %, while TS and PR have the units of K and mm day$^{-1}$, respectively.

**Table 3:** The radiative and turbulent fluxes averaged over Indian landmass (land points only: 75°-90°E, 5°-25°N) for JJAS season. Fluxes are signed in the direction of the fluxes (i.e. negative sign indicates upward fluxes and vice-versa). Asterisk (*) in Table represents that the rainfall (PR) is averaged using the GPCP data and not using ERAi estimates. All fluxes have energy units (Wm$^{-2}$) and albedo is in %, while TS and PR have the units of K and mm day$^{-1}$, respectively.

**Table 4:** The radiative and turbulent fluxes averaged over the land points in the hot subtropical desert domain (15°-40°N and 20°W-75°E) during JJAS season for the negative albedo perturbation experiments. Asterisk (*) in Table indicates that the flux values are averaged only

over 15°-40°N and 35°-75°E (e.g. in the Desert_Arab_m20 experiment). Fluxes are signed in the direction of the fluxes (i.e. negative sign indicates upward fluxes and vice-versa). The upper part of the Table provides the climatological estimates from the sensitivity experiments while the lower part shows the anomalous responses (deviations from the CTRL climatology, see Section 2). All fluxes have energy units ($Wm^{-2}$) and albedo is in %, while TS and PR have the units of K and mm $day^{-1}$, respectively.

**Table 5:** The radiative and turbulent fluxes averaged over Indian landmass (land points only: 75°-90°E, 5°-25°N) during JJAS season for the negative albedo perturbation experiments. Fluxes are signed in the direction of the fluxes (i.e. negative sign indicates upward fluxes and vice-versa). The upper part of the Table provides the climatological estimates from the sensitivity experiments while the lower part shows the anomalous responses (deviations from the CTRL climatology). All fluxes have energy units ($Wm^{-2}$) and albedo is in %, while TS and PR have the units of K and mm $day^{-1}$, respectively.

**Table 6:** The radiative and turbulent fluxes averaged over the hot subtropical desert domain during JJAS season for the positive albedo perturbation experiments. Asterisk (*) in Table indicates that the flux values are averaged only over 15°-40°N and 35°-75°E (e.g. in the Desert_Arab_p20 experiment). Fluxes are signed in the direction of the fluxes (i.e. negative sign indicates upward fluxes and vice-versa). The upper part of the Table provides the climatological estimates from the sensitivity experiments while the lower part shows the anomalous responses (deviations from the CTRL climatology). All fluxes have energy units ($Wm^{-2}$) and albedo is in %, while TS and PR have the units of K and mm $day^{-1}$, respectively.

**Table 7:** The radiative and turbulent fluxes averaged over Indian landmass (land points only: 75°-90°E, 5°-25°N) during JJAS season for the positive albedo perturbation experiments. Fluxes

are signed in the direction of the fluxes (i.e. negative sign indicates upward fluxes and vice-versa). The upper part of the Table provides the climatological estimates from the sensitivity experiments while the lower part shows the anomalous responses (deviations from the CTRL climatology, see Section 2). All fluxes have energy units ($Wm^{-2}$) and albedo is in %, while TS and PR have the units of K and mm $day^{-1}$, respectively.

**Figures:**

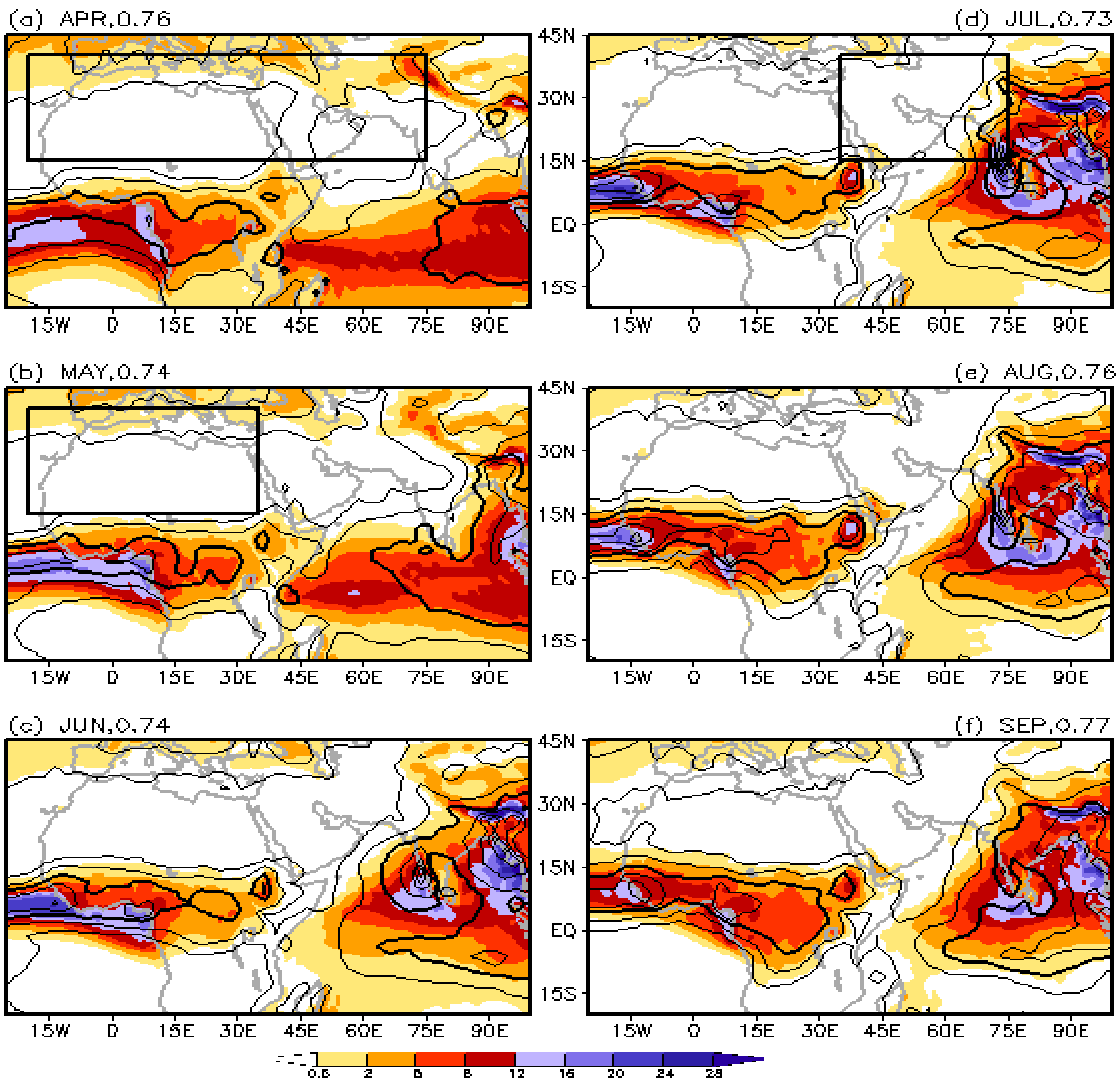


**Figure 1:** Spatio-temporal evolution of rainfall climatology (mm day$^{-1}$) for May to September. The overlying contours represent rainfall estimates from GPCP, while shading is the same from CTRL (control simulation). The contours are drawn following the shading convention and the 5 mm day$^{-1}$ contour is highlighted in thick black colour. The pattern correlation between CTRL and GPCP for the tropical domain (i.e. within 20°S to 35°N) is indicated in each panel. The boxed area in (a), (b) and (d) represent the hot subtropical deserts regions where artificial albedo perturbation experiments are carried out (see Table 1 for more details).

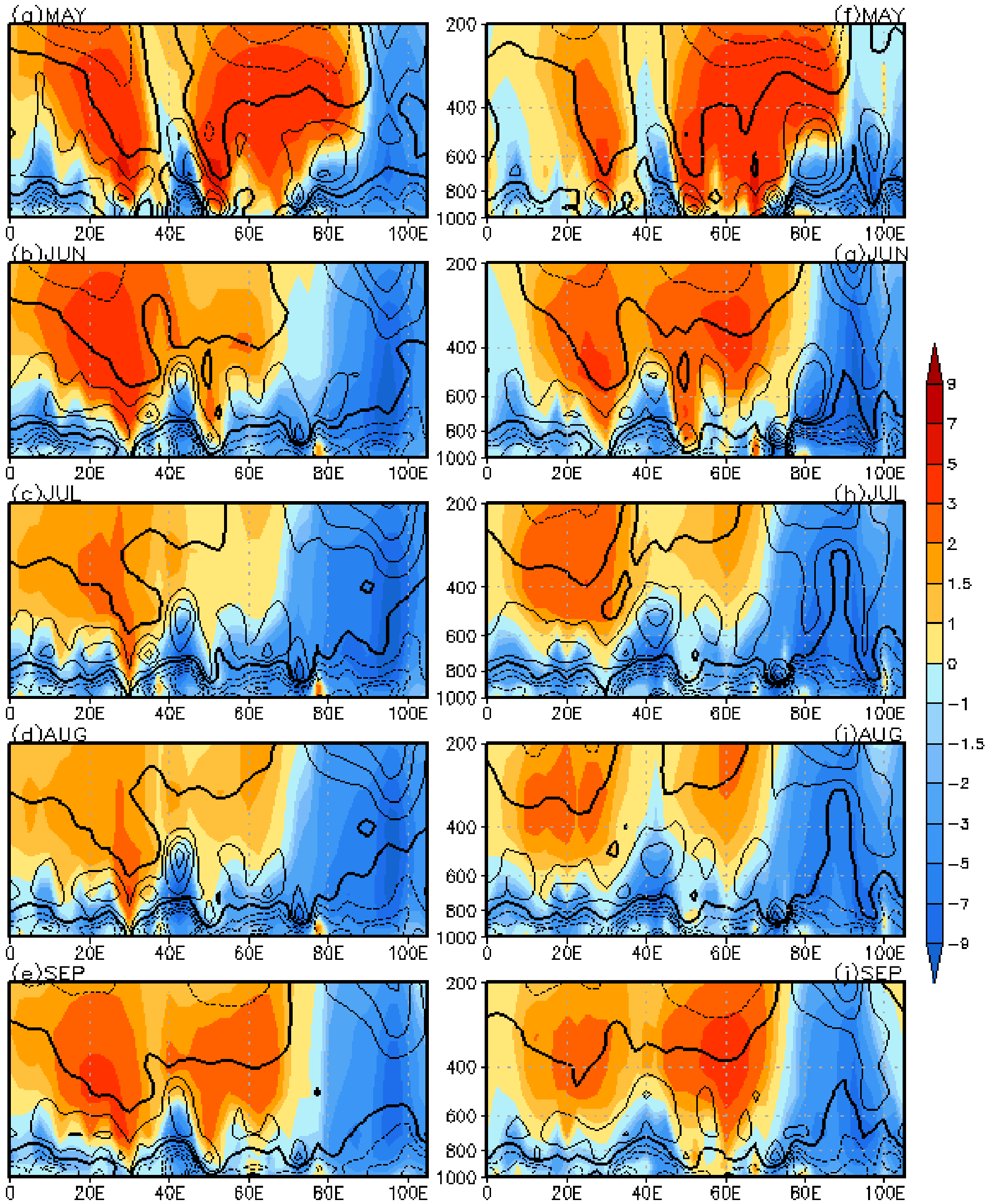


**Figure 2:** Seasonal evolution (May to September) of vertical component of velocity (shading, units in $10^{-2}$ Pa $s^{-1}$) and horizontal divergence (contours, units in $10^{-6}s^{-1}$), along a pressure-longitude plane averaged over 15°-30°N for ERAi (left panel, a-e) and CTRL (right panel, f-j). The negative (dashed) and positive (continuous) contours correspond, respectively, to absolute magnitudes of 1, 2, 3 and 4 units. The zero contours are highlighted in thick black colour.

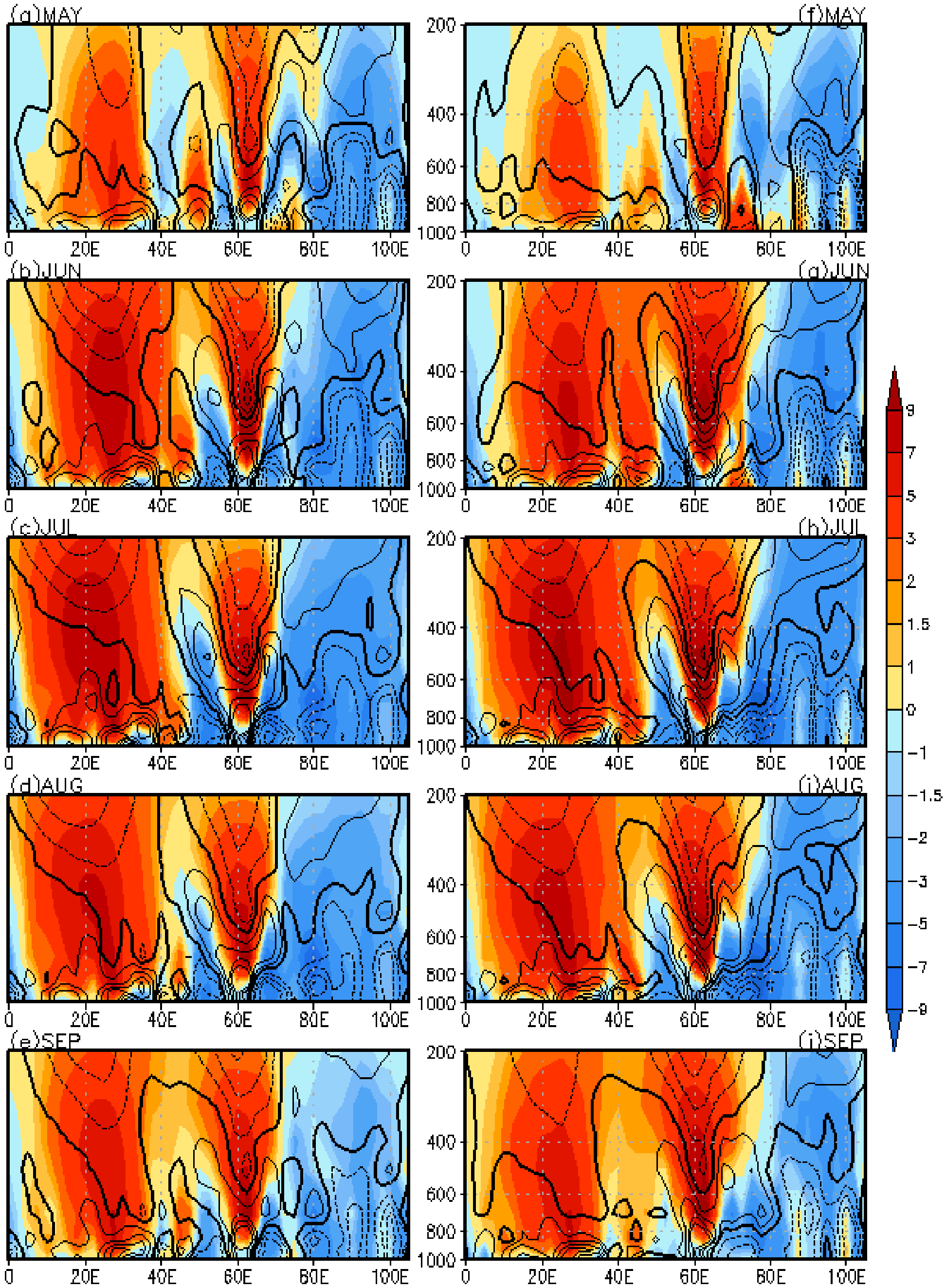


**Figure 3 (a-j):** Same Figure 2, but for the vertical component of velocity (shading, units in $10^{-2}$ Pa $s^{-1}$) and horizontal divergence (contours, units in $10^{-6}$ $s^{-1}$), averaged over 30°-40°N. The negative (dashed) and positive (continuous) contours correspond, respectively, to absolute magnitudes of 1, 2, 3 and 4 units. The zero contours are highlighted in thick black colour.

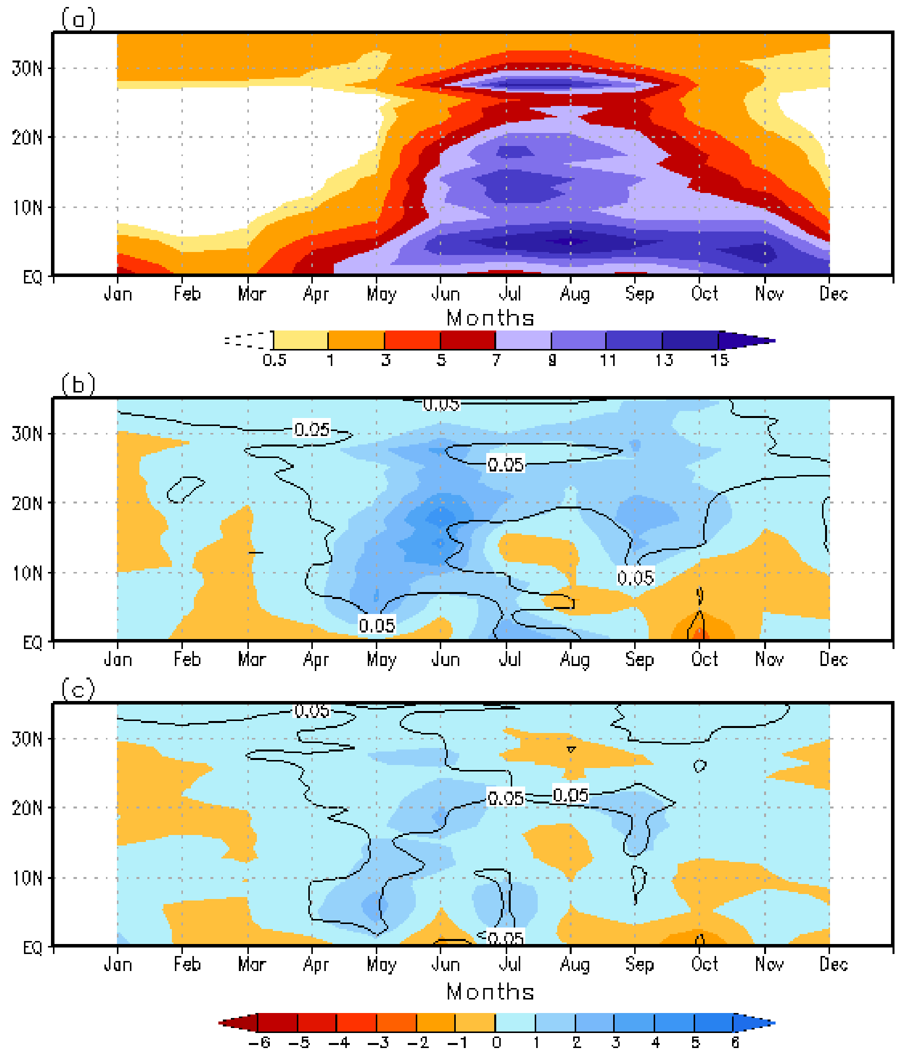


**Figure 4:** (a) Time-latitude evolution of rainfall climatology (mm day$^{-1}$, containing both land and oceanic points) averaged along 70°-90°E, from CTRL. (b) and (c) time-latitude evolution of anomalous rainfall response (computed against the CTRL rainfall climatology, see Section 2) averaged along 70°-90°E from Desert_m20 and from Desert_Arab_m20, respectively. In (b) and (c), the responses that are above the 95% confidence level according to a permutation procedure with 9999 shuffles are encircled.

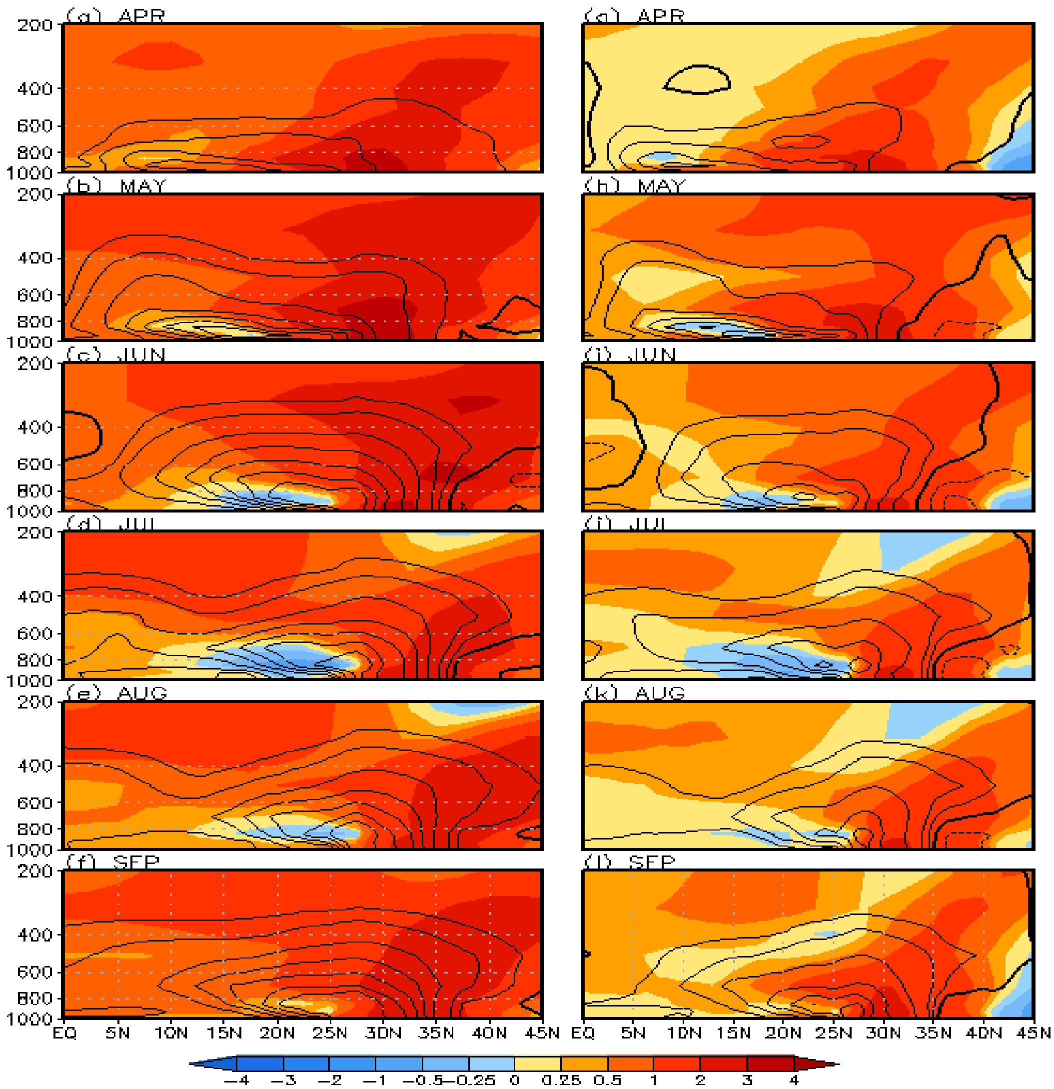


**Figure 5:** (Left Panel, a-f) Seasonal evolution (April to September) of response in temperature (shading, °C) and specific humidity (contours, x$10^{-3}$ Kg $Kg^{-1}$) along a pressure-latitude plane over the longitudes 55°-75°E, for Desert_m20 experiment. Right panel (g-l), same as (a-f), but for Desert_Arab_m20 experiment. The anomalous responses are computed against the CTRL climatology (see Section 2). The negative (dashed) and positive (continuous) contours correspond, respectively, to absolute magnitudes of 0.25, 0.5, 1, 1.5, 2, 2.5 and 3 units. The zero contours are highlighted in thick black colour.

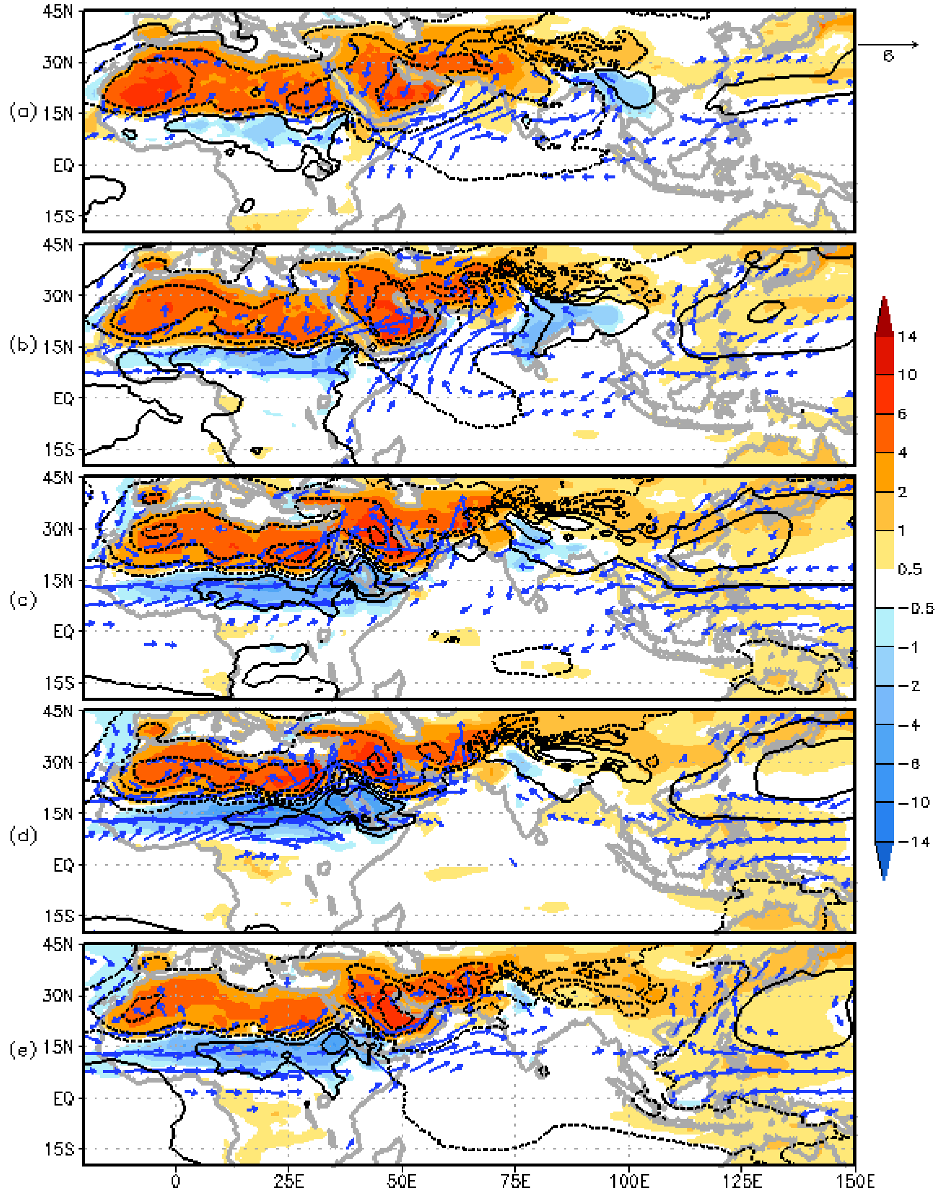


**Figure 6:** Seasonal evolution (May to September) of response in MSLP (contours, hPa), TS (shading, °C) and 850-hPa wind ($ms^{-1}$) from Desert_m20 experiment. Negative (dashed) and positive (continuous) contours correspond respectively to magnitudes of 0.5, 1.5, 3, 4 and 6 units. The zero contours are not drawn. The anomalous response is computed against the CTRL climatology (see Section 2). Wind vectors of magnitudes exceeding 1 $ms^{-1}$ are only drawn.

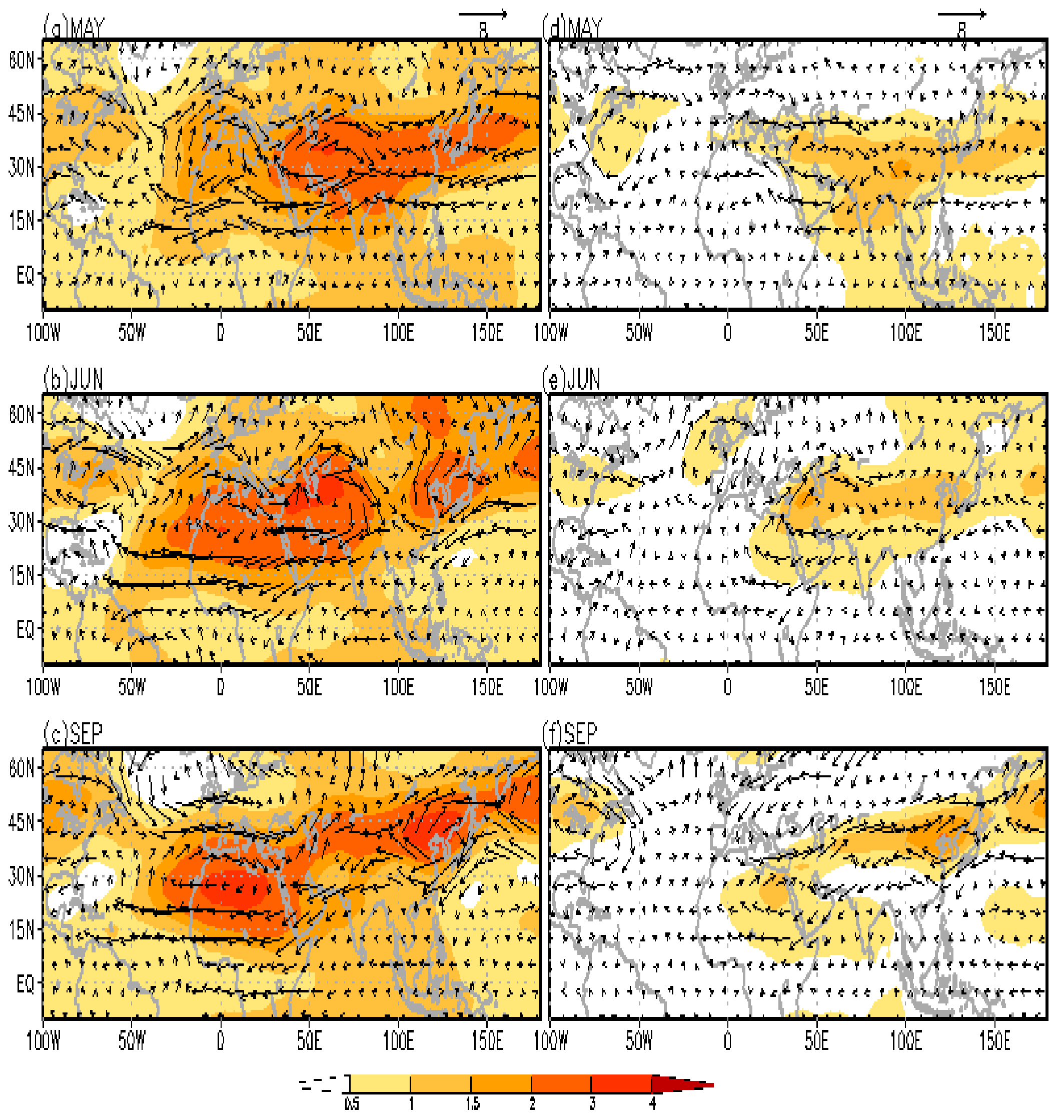


**Figure 7**: Map of the anomalous responses in wind and temperature at 300-hPa for (a) May, (b) June and (c) September, from Desert_m20 experiments. (d)-(f), same as (a)-(c), but from Desert_Arab_m20. The anomalous response is against the CTRL climatology (see Section 2).

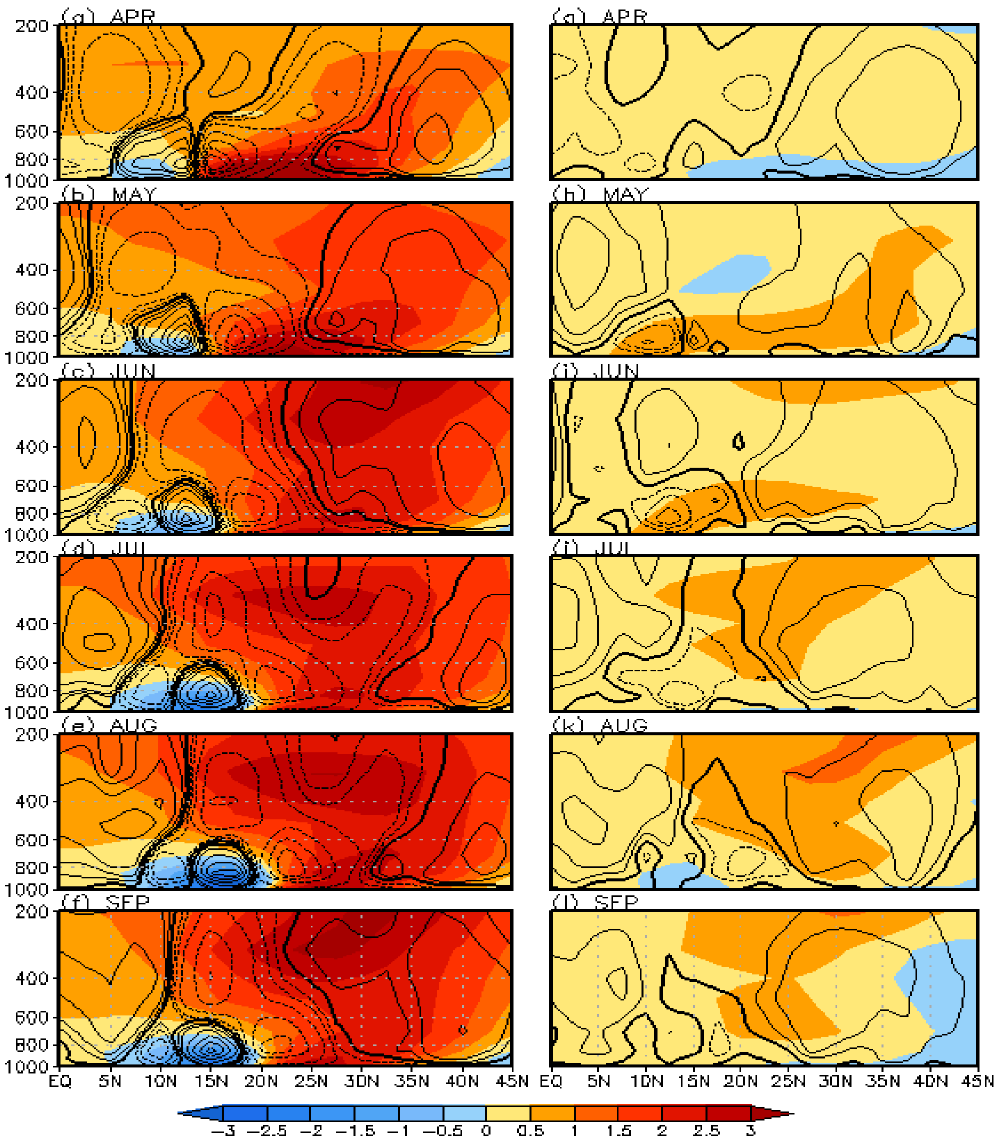


**Figure 8:** (Left Panel, a-f) Seasonal evolution (April to September) of response in temperature (shading, °C) and vertical component of velocity (contours, units is $10^{-2}$ Pa $s^{-1}$) along a pressure-latitude plane averaged over the longitudes 20°W-30°E, for Desert_m20 experiment. Right panel (g-l), same as (a-f), but for Desert_Arab_m20 experiment. The anomalous response is computed against the CTRL climatology (see Section 2). The negative (dashed) and positive (continuous) contours correspond respectively to magnitudes of 0.25, 0.5, 1, 2, 3, 4 and 5 units. The zero contours are highlighted in thick black colour.

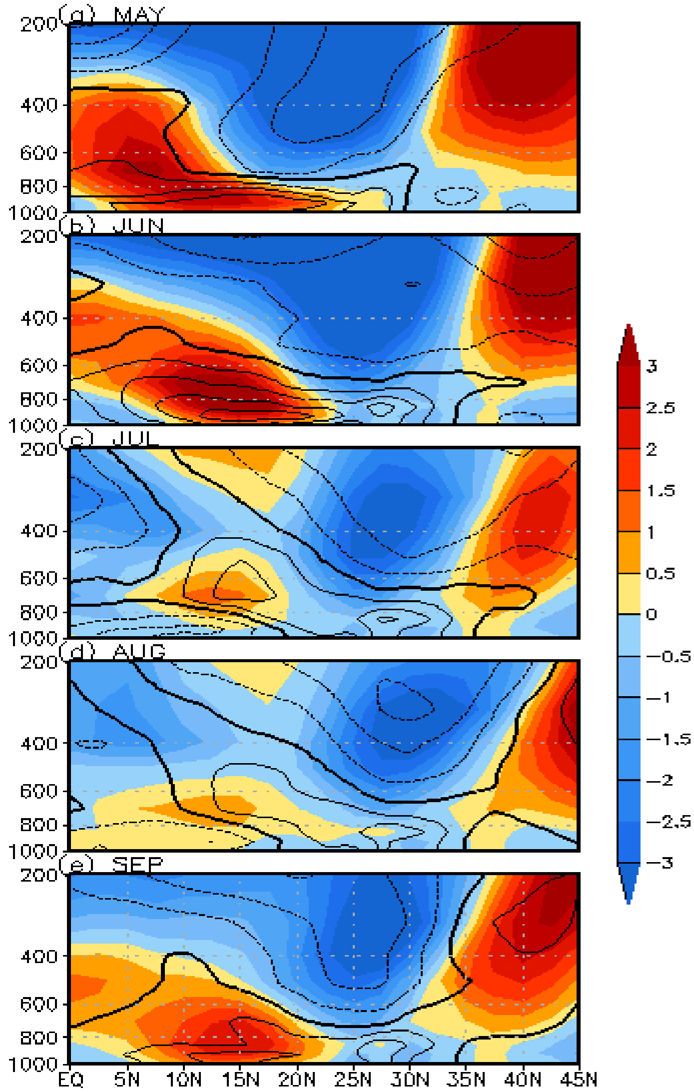


**Figure 9: S**easonal evolution (May to September) of response in horizontal component of wind (zonal wind in shading and meridional wind in contours, $ms^{-1}$) along a pressure-latitude plane averaged over the longitudes 55°-75°E, for Desert_m20 experiment. The anomalous response is computed against the CTRL climatology (see Section 2). The negative (dashed) and positive (continuous) contours correspond respectively to magnitudes of 0.5, 1, 1.5, 2, 2.5 and 3 units. The zero contours are highlighted in thick black colour.

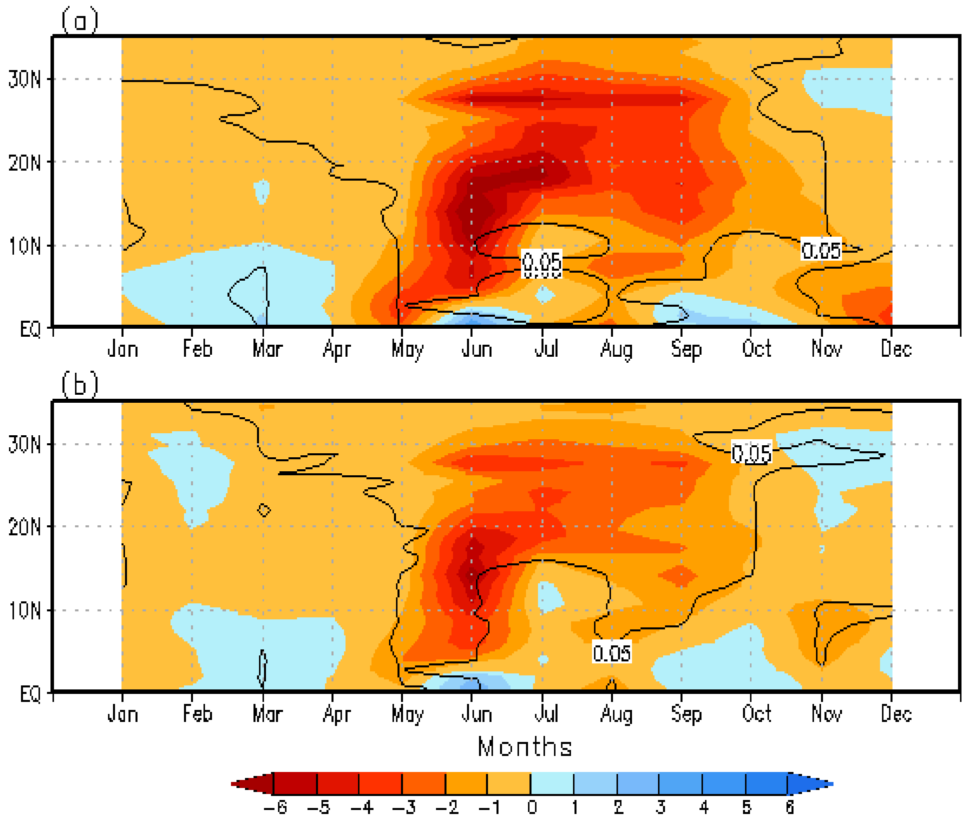


**Figure 10:** Time-latitude evolution of rainfall response (mm day$^{-1}$, averaged along 70°-90°E from the sensitivity experiments. In (a) from Desert_p20 and in (b) from Desert_Arab_p20. The anomalous responses are computed against the CTRL climatology (see Section 2). In all panels, the responses that are above the 95% confidence level according to a permutation procedure with 9999 shuffles are encircled.

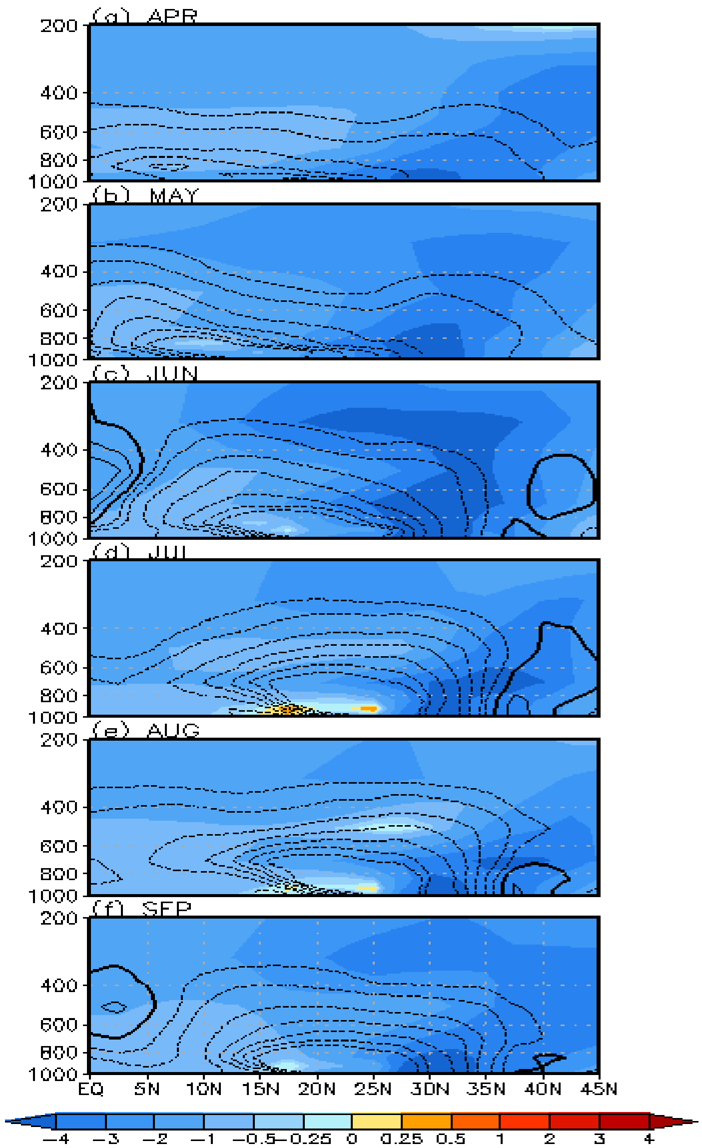


**Figure 11:** Seasonal evolution (April to September) of response in temperature (shading, °C) and specific humidity (contours, x$10^{-3}$ Kg $Kg^{-1}$) along a pressure-latitude plane over the longitudes 55°-75°E, for Desert_p20 experiment. The anomalous response is computed against the CTRL climatology (see Section 2). The negative (dashed) and positive (continuous) contours correspond, respectively, to magnitudes of 0.25, 0.5, 1, 1.5, 2, 2.5 and 3 units. The zero contours are highlighted in thick black colour.

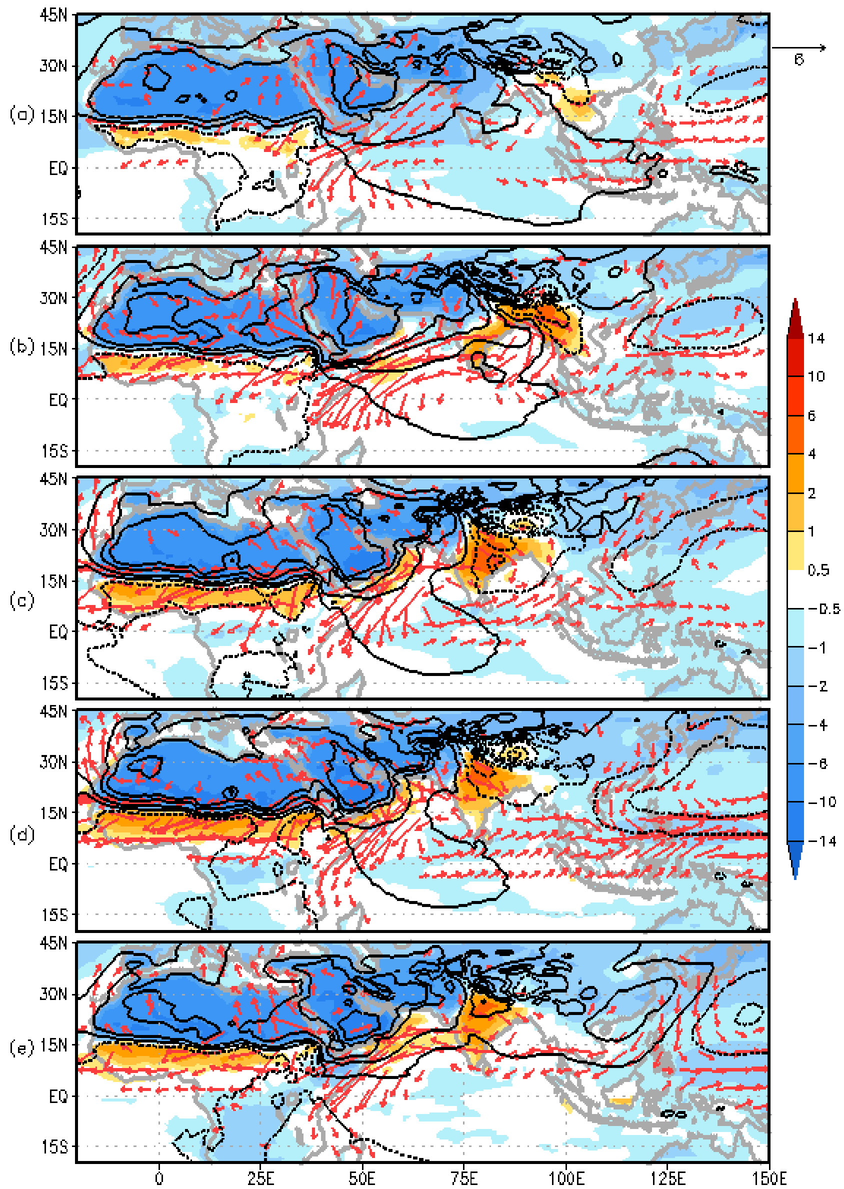


**Figure 12:** Seasonal evolution (May to September) of response in MSLP (contours, hPa), TS (shading, °C) and 850-hPa wind (ms$^{-1}$) from Desert_p20 experiment. Negative (dashed) and positive (continuous) contours correspond respectively to magnitudes of 0.5, 1.5, 3, 4 and 6 units. The zero contours are not drawn. The anomalous response is computed against the CTRL climatology (see Section 2). Wind vectors of magnitudes exceeding 1 ms$^{-1}$ are only drawn.

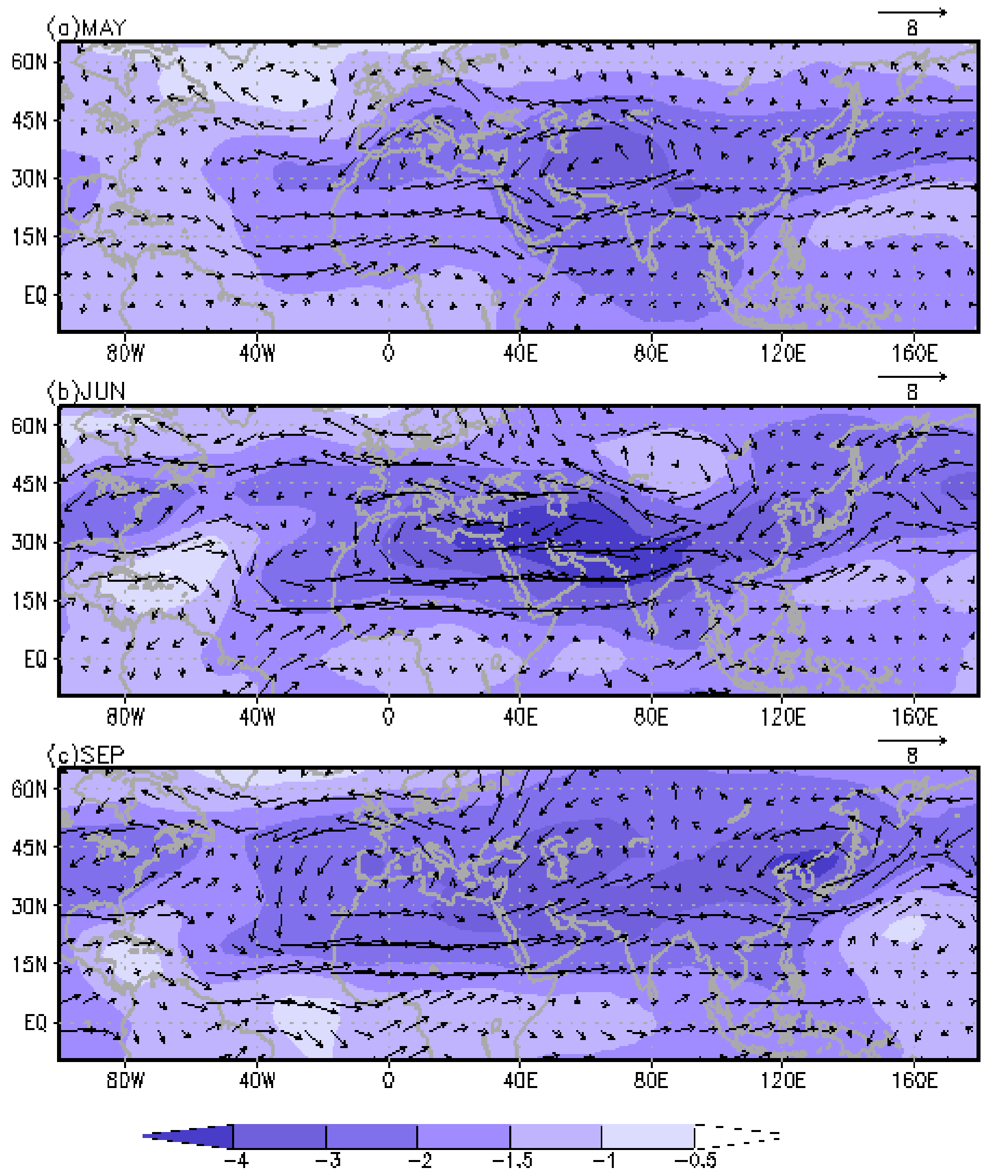


**Figure 13:** (a) Anomalous response in wind ($ms^{-1}$) and temperature (°C, shading) at 300-hPa, during May from Desert_p20 experiment. (b) and (c), same as (a), but for June and September, respectively. The anomalous response is computed against the CTRL climatology (see Section 2).

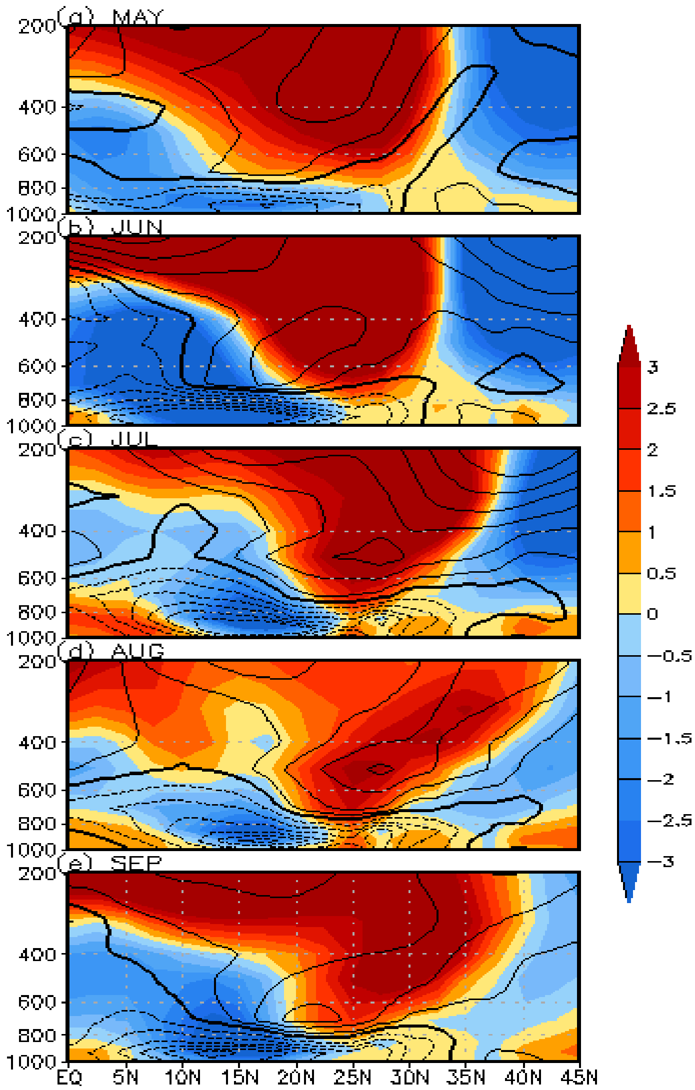


**Figure 14: S**easonal evolution (May to September) of response in horizontal component of wind (zonal wind in shading and meridional wind in contours, $ms^{-1}$) along a pressure-latitude plane averaged over the longitudes 55°-75°E, for Desert_p20 experiment. The anomalous response is computed against the CTRL climatology (see Section 2). The negative (dashed) and positive (continuous) contours correspond, respectively, to magnitudes of 0.5, 1, 1.5, 2, 2.5 and 3 units. The zero contours are highlighted in thick black colour.

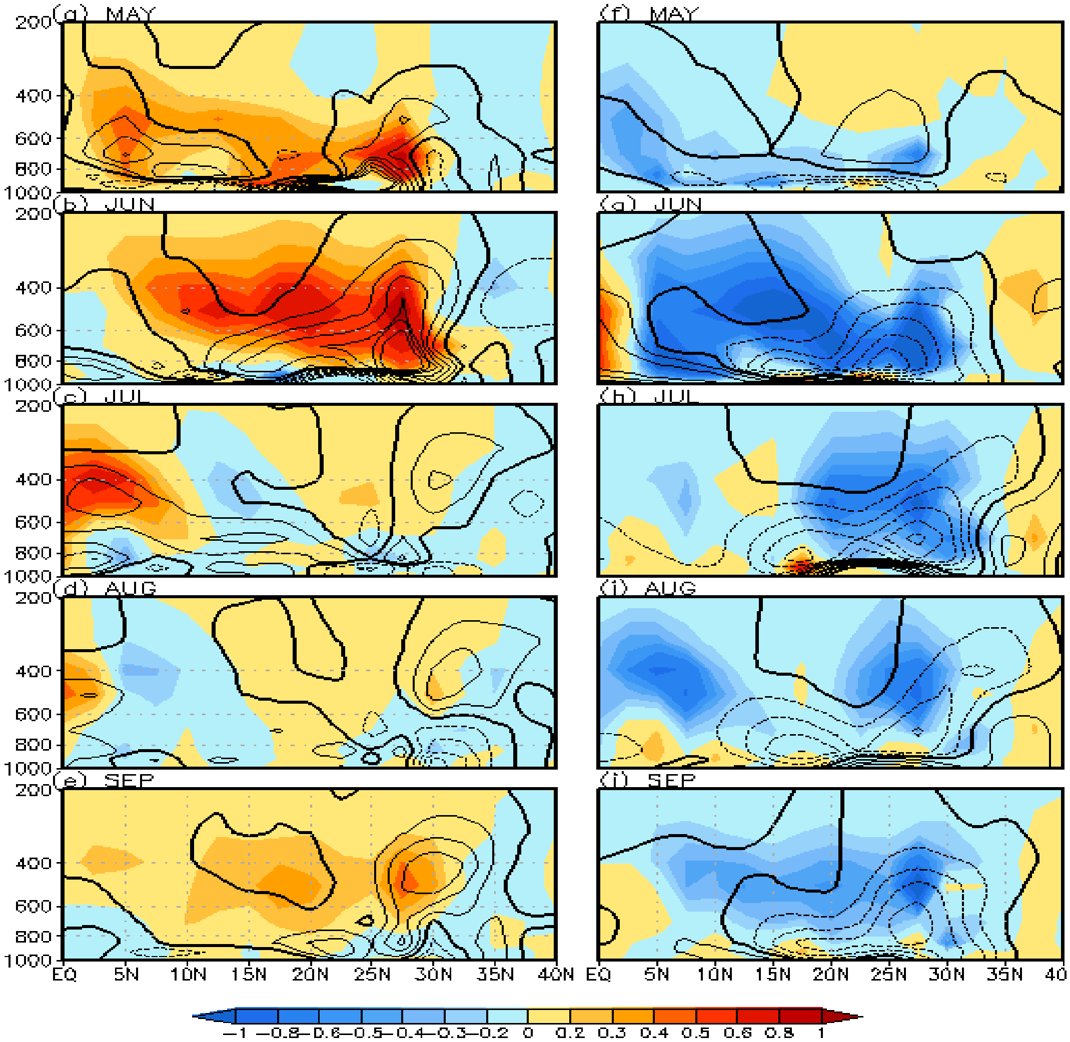


**Figure 15:** (Left Panel, a-e) Seasonal evolution (May to September) of response in vertical moisture advection (shading, units is $10^{-3}$ Kg $Kg^{-1}$ $day^{-1}$) and horizontal moisture advection (contours, $x10^{-3}$ Kg $Kg^{-1}$ $day^{-1}$) along a pressure-latitude plane over the longitudes 75°-90°E, for Desert_m20 experiment. Right panel (f-j), same as (a-e), but for Desert_p20 experiment. The anomalous response is computed against the CTRL climatology (see Section 2). The negative (dashed) and positive (continuous) contours correspond respectively to magnitudes of 0.1, 0.2, 0.3, 0.4, 0.5 and 0.6 units. The zero contours are highlighted in thick black colour.

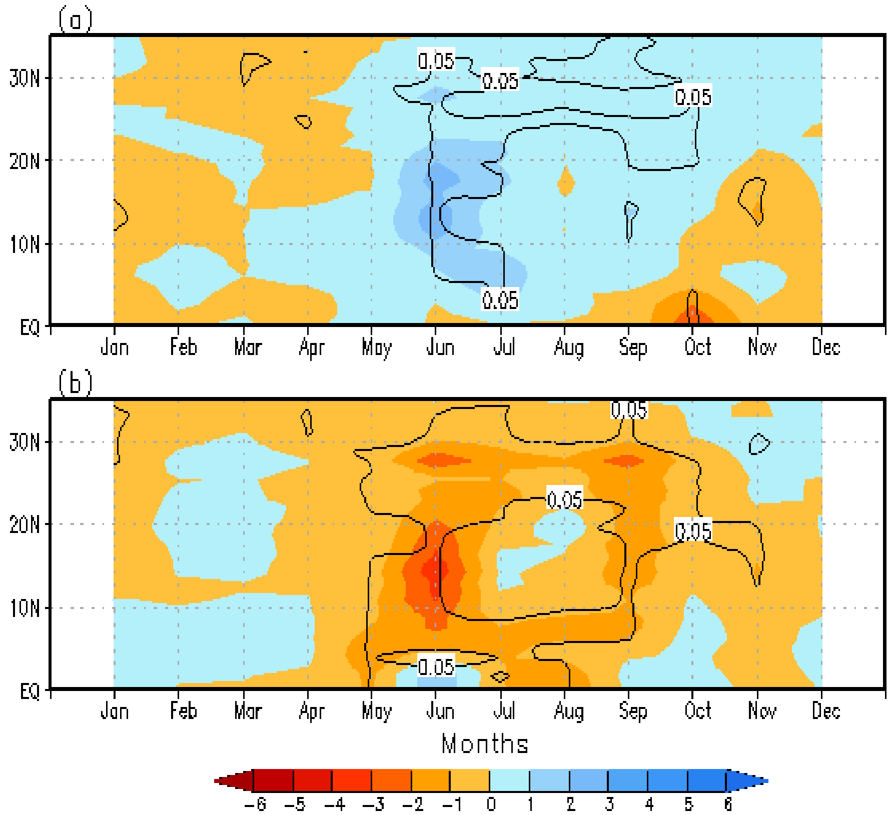


**Figure 16:** (a) Time-latitude evolution of rainfall response (mm day$^{-1}$, averaged along 70°-90°E from the Desert_Sahara_m20 experiment. In (b), same as (a) but for Desert_Sahara_p20 experiment. The anomalous responses are computed against the CTRL climatology (see Section 2). In (a) and (b), the responses that are above the 95% confidence level according to a permutation procedure with 9999 shuffles are encircled.

**Supplementary Figures:**

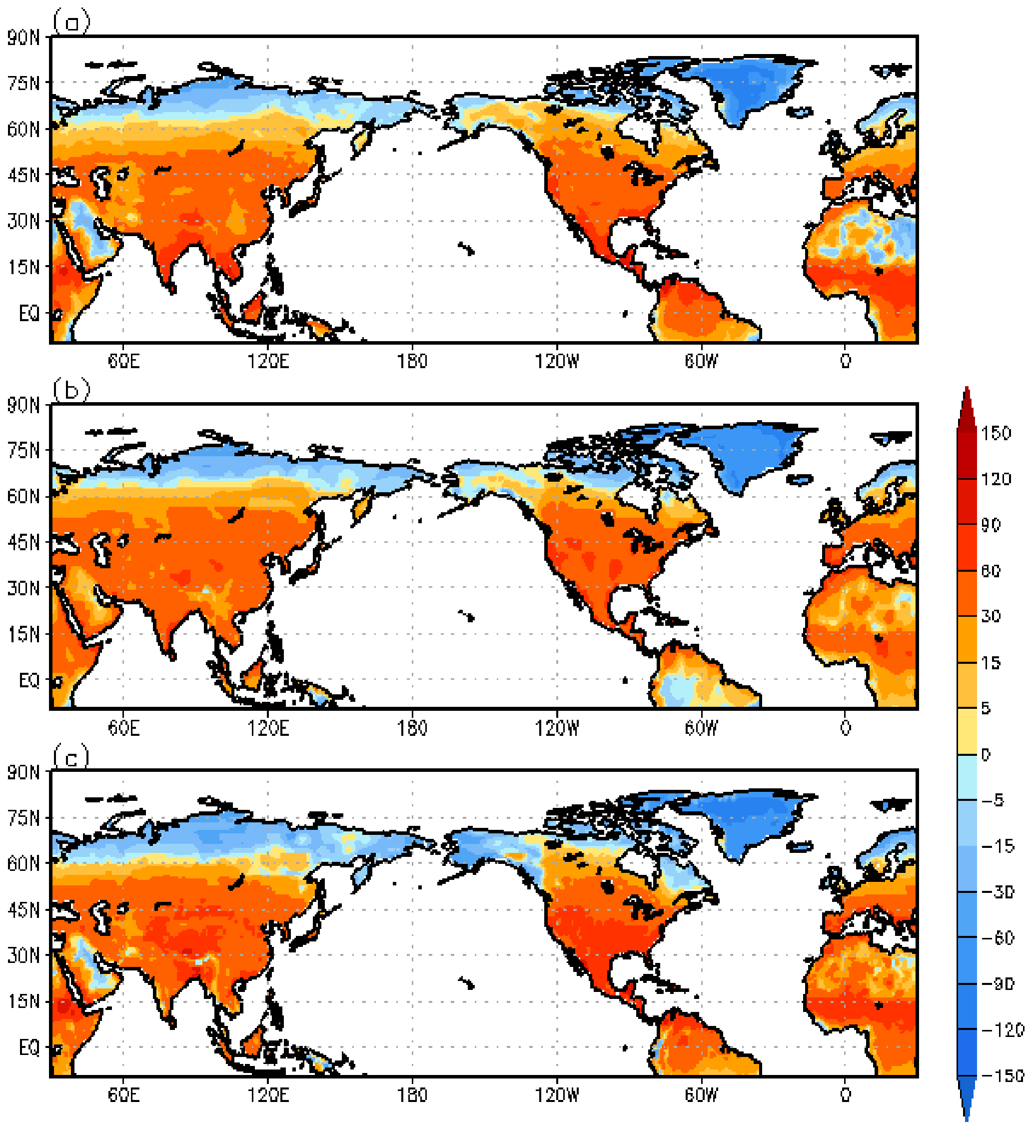


**Figure S1:** Climatological map of net radiation budget at TOA ($Wm^{-2}$, see Table 2 and Section 2 for more details on radiation budget) for June to September period. In (a). CERES-EBAF, (b) ERAi and (c) CTRL

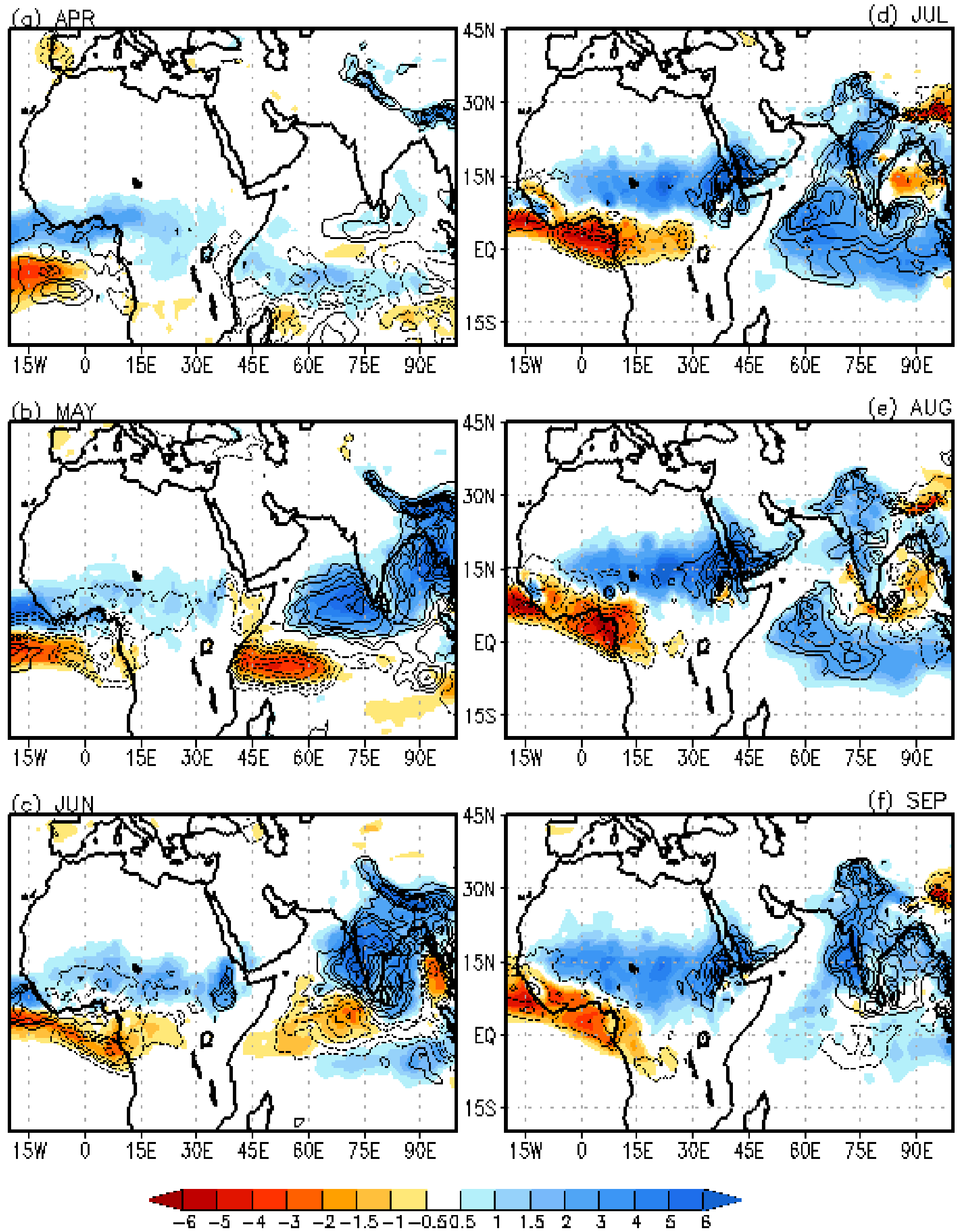


**Figure S2:** Spatio-temporal evolution of rainfall (May to September, mm day$^{-1}$) response from the Desert_m20 experiment (in shading). The overlying contours are the rainfall response from Desert_Arab_m20. Negative (dashed) and positive (continuous) contours are drawn following the shading convention. The anomalous responses are computed against the CTRL climatology (see Section 2).

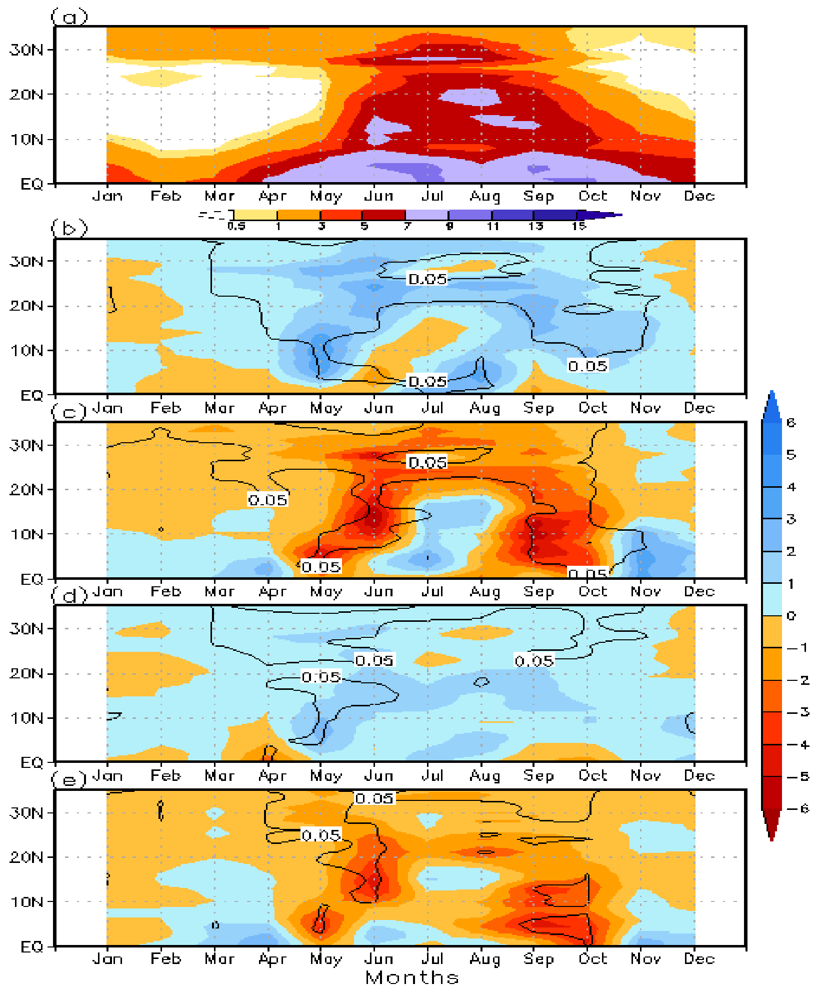


**Figure S3:** In (a) to (c), same as that of Figure 4, but for the various experiments (CTRL, Desert_m20 and Desert_p20), conducted using CFSv2 coupled model (see Terray et al. 2017). Similarly, in (d) and (e), same as that of Figure 11, but for Desert_Arab_m20 and Desert_Arab_p20 simulations, using CFSv2. The length of integration (i.e. using CFSv2) in CTRL simulation is for 40 years, while it is 20 years for the Desert_m20 and Desert_p20. Note that the configuration used for the experiments also takes advantage of up-to-date satellite MODIS data for estimating the background snow-free albedo as described in Terray et al. (2017). The first 10 years of all the simulations are excluded for all the analyses presented in the text. In (b) and (c), the responses that are above the 95% confidence level according to a permutation procedure with 9999 shuffles are encircled.

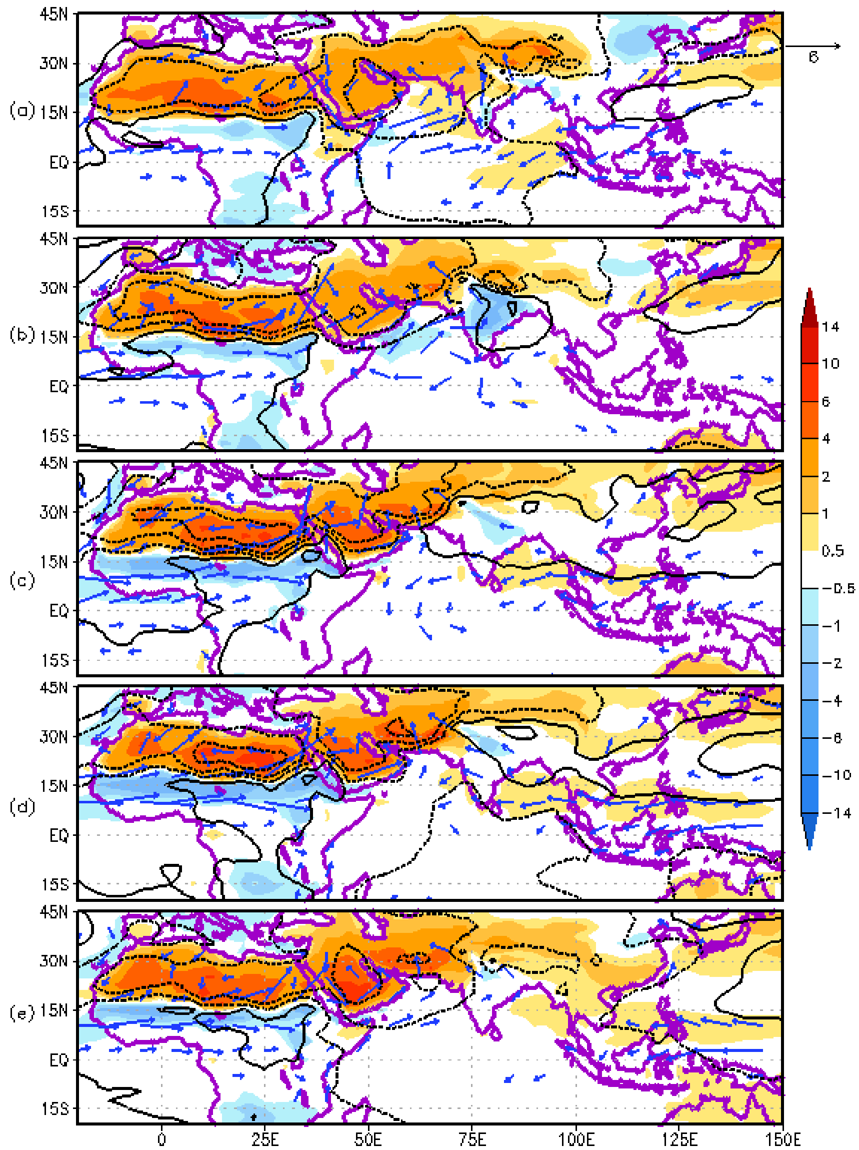


**Figure S4**: Seasonal evolution (May to September) of response in MSLP (contours, hPa), TS (shading, °C) and 850-hPa wind ($ms^{-1}$) from Desert_m20 experiment done using CFSv2 model. Negative (dashed) and positive (continuous) contours correspond respectively to magnitudes of 0.5, 1.5, 3, 4 and 6 units. The anomalous response is computed against the CTRL climatology. Wind vectors of magnitudes exceeding 1 $ms^{-1}$ are only drawn. For more details of the CFS runs, please refer to the legend of Fig. S3.

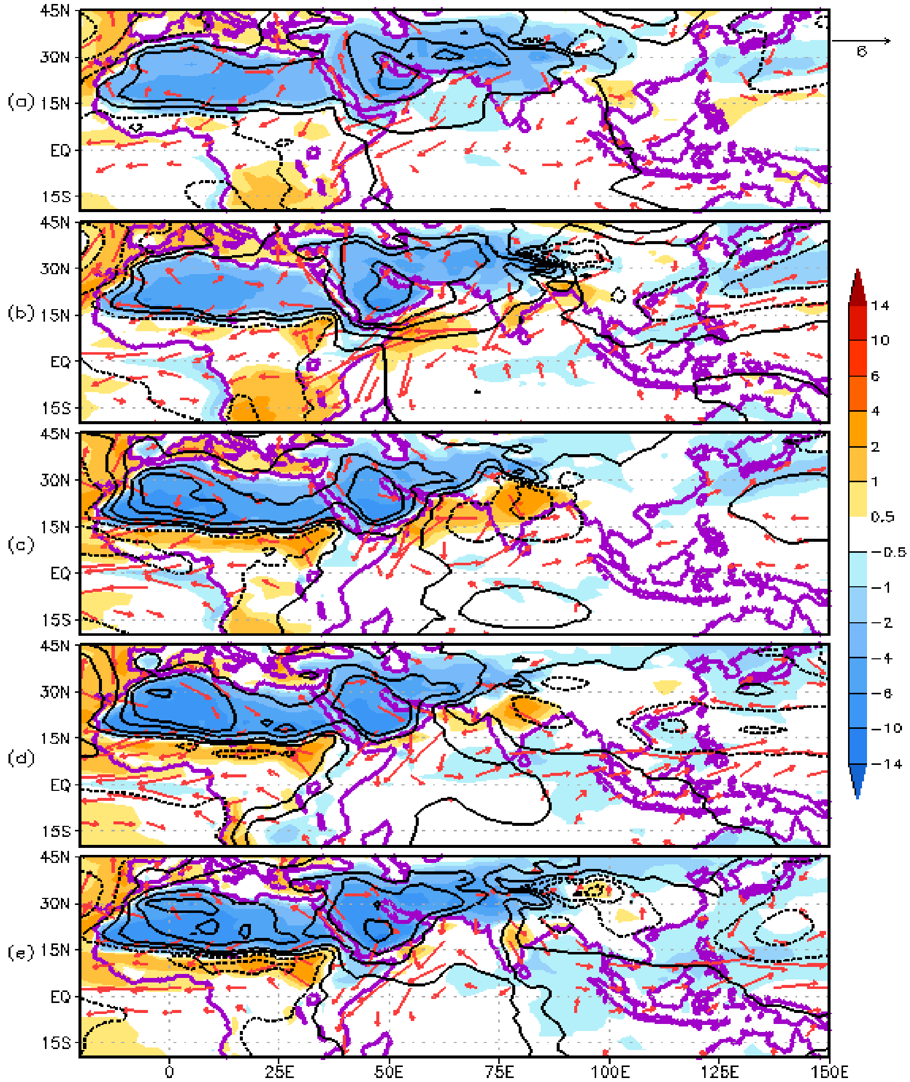


**Figure S5:** Seasonal evolution (May to September) of response in MSLP (contours, hPa), TS (shading, °C) and 850-hPa wind (ms$^{-1}$) from Desert_p20 experiment done using CFSv2 model. Negative (dashed) and positive (continuous) contours correspond respectively to magnitudes of 0.5, 1.5, 3, 4 and 6 units. The anomalous response is computed against the CTRL climatology. Wind vectors of magnitudes exceeding 1 ms$^{-1}$ are only drawn. For more details of the CFS runs, please refer to the legend of Fig. S3.

**Table 1:** Details of coupled model experiments as performed using SINTEX-F2 coupled model. The first 10 years of all the simulations are excluded for all the analyses presented in the text. See Section 2 for more details of the experiments.

| Experiment name | Length of integration (years) | Experimental setup |
|---|---|---|
| CTRL | 110 | Control experiment using background snow-free broadband shortwave albedo prescribed from MODIS products (Terray et al. 2017) |
| Desert_m20 | 60 | Similar to CTRL with the exception that the background land MODIS albedo has been artificially decreased by -20% over the hot subtropical desert (15°-40°N, 20°W-75°E) |
| Desert_p20 | 60 | Same as Desert_m20, but with an increase in background albedo of +20% over the hot subtropical desert (15°-40°N, 20°W-75°E) |
| Desert_Arab_m20 | 60 | Similar to CTRL, but with a decrease in background albedo of -20% over the Arabia and Middle-East deserts only (15°-40°N, 35°E-75°E) |
| Desert_Arab_p20 | 60 | Same as Desert_Arab_m20, but with an increase in background albedo of +20% over the Arabia and Middle-East deserts (15°-40°N, 35°E-75°E) |
| Desert_Sahara_m20 | 60 | Similar to CTRL, but with a decrease in background albedo of -20% over the Sahara desert only (15°-40°N, 20°W-35°E) |
| Desert_Sahara_p20 | 60 | Same as Desert_Sahara_m20, but with an increase in background albedo of +20% over the Sahara desert (15°-40°N, 20°W-35°E) |

**Table 2:** The radiative and turbulent fluxes, at surface (SURF) and top of the atmosphere (TOA), averaged over the land points in the domain 15°-40°N and 20°W-75°E (e.g. hot subtropical desert region) for June to September (JJAS) season. Here, SW and LW are shortwave and long-wave radiations, respectively. Net Rad means net radiation following the formulation in Su and Neelin (2002). SH and LH are sensible and latent heat fluxes. TS and PR stands for surface skin temperature and rainfall, respectively. Fluxes are signed in the direction of the fluxes (i.e. negative sign indicates upward fluxes and vice-versa). Asterisk ($^{*}$) in the Table represents that the rainfall (PR) is averaged using the GPCP data and not using ERAi estimates. All fluxes have energy units ($Wm^{-2}$) and albedo is in %, while TS and PR have the units of K and mm $day^{-1}$, respectively.

| | Albedo at TOA (SURF) | Net SW at TOA (SURF) | LW at TOA (SURF) | Net LW at TOA (SURF) | Net Rad at TOA (SURF) | LH Flux | SH flux | TS | PR$^{*}$ |
|---|---|---|---|---|---|---|---|---|---|
| ERAi | 26 (28) | 330 (211) | -300 (-494) | -300 (-119) | 30 (92) | -19 | -69 | 305.8 | 0.5 |
| CERES-EBAF | 29 (29) | 310 (206) | -294 (-501) | -294 (-111) | 16 (95) | | | | |
| CTRL | 28 (30) | 323 (202) | -294 (-497) | -294 (-116) | 29 (86) | -9 | -73 | 305.6 | 0.3 |

**Table 3:** The radiative and turbulent fluxes averaged over Indian landmass (land points only: 75°-90°E, 5°-25°N) for JJAS season. Fluxes are signed in the direction of the fluxes (i.e. negative sign indicates upward fluxes and vice-versa). Asterisk (*) in Table represents that the rainfall (PR) is averaged using the GPCP data and not using ERAi estimates. All fluxes have energy units ($Wm^{-2}$) and albedo is in %, while TS and PR have the units of K and mm $day^{-1}$, respectively.

| | Albedo at TOA (SURF) | Net SW at TOA (SURF) | LW at TOA (SURF) | Net LW at TOA (SURF) | Net Rad at TOA (SURF) | LH Flux | SH flux | TS | PR* |
|---|---|---|---|---|---|---|---|---|---|
| ERAi | 34 (17) | 290 (155) | -237 (-460) | -237 (-39) | 53 (116) | -92 | -27 | 300.4 | 7.7 |
| CERES-EBAF | 35 (14) | 284 (167) | -216 (-461) | -216 (-36) | 68 (131) | | | | |
| CTRL | 39 (16) | 269 (154) | -223 (-474) | -223 (-41) | 46 (113) | -68 | -47 | 302.3 | 6 |

**Table 4:** The radiative and turbulent fluxes averaged over the land points in the hot subtropical desert domain (15°-40°N and 20°W-75°E) during JJAS season for the negative albedo perturbation experiments. Asterisk (*) in Table indicates that the flux values are averaged only over 15°-40°N and 35°-75°E (e.g. in the Desert_Arab_m20 experiment). Fluxes are signed in the direction of the fluxes (i.e. negative sign indicates upward fluxes and vice-versa). The upper part of the Table provides the climatological estimates from the sensitivity experiments while the lower part shows the anomalous responses (deviations from the CTRL climatology, see Section 2). All fluxes have energy units ($Wm^{-2}$) and albedo is in %, while TS and PR have the units of K and mm $day^{-1}$, respectively.

| | Albedo at TOA (SURF) | Net SW at TOA (SURF) | LWat TOA (SURF) | Net LW at TOA (SURF) | Net Rad at TOA (SURF) | LH Flux | SH flux | TS | PR |
|---|---|---|---|---|---|---|---|---|---|
| | | Climatological responses | | | | | | | |
| Desert_m20 | 22 (11) | 348 (233) | -280 (-516) | -280 (-110) | 68 (123) | -17 | -102 | 308.5 | 0.8 |
| *Desert_Arab_m20 | 19 (7) | 361 (255) | -293 (-509) | -293 (-119) | 68 (136) | -16 | -115 | 307.3 | 0.6 |
| | | Anomalous responses | | | | | | | |
| Desert_m20 | -6 (-19) | 25 (31) | 14 (-19) | 14 (6) | 39 (37) | -8 | -29 | 2.9 | 0.5 |
| *Desert_Arab_m20 | -7 (-19) | 30 (36) | 10 (-17) | 10 (0) | 40 (36) | -2 | -33 | 2.6 | 0.25 |

**Table 5:** The radiative and turbulent fluxes averaged over Indian landmass (land points only: 75°-90°E, 5°-25°N) during JJAS season for the negative albedo perturbation experiments. Fluxes are signed in the direction of the fluxes (i.e. negative sign indicates upward fluxes and vice-versa). The upper part of the Table provides the climatological estimates from the sensitivity experiments while the lower part shows the anomalous responses (deviations from the CTRL climatology). All fluxes have energy units ($Wm^{-2}$) and albedo is in %, while TS and PR have the units of K and mm $day^{-1}$, respectively.

| | Albedo at TOA (SURF) | Net SW at TOA (SURF) | LWat TOA (SURF) | Net LW at TOA (SURF) | Net Rad at TOA (SURF) | LH Flux | SH flux | TS | PR |
|---|---|---|---|---|---|---|---|---|---|
| | | Climatological responses | | | | | | | |
| Desert_m20 | 42 (16) | 256 (138) | -214 (-470) | -214 (-32) | 42 (106) | -78 | -31 | 301.6 | 8 |
| Desert_Arab _m20 | 41 (16) | 261 (145) | -219 (-471) | -219 (-36) | 42 (109) | -72 | -37 | 302 | 7 |
| | | Anomalous responses | | | | | | | |
| Desert_m20 | 3 (0) | -13 (-16) | 9 (4) | 9 (9) | -4 (-7) | -10 | 16 | -0.7 | 2 |
| Desert_Arab _m20 | 2 (0) | -8 (-9) | 4 (3) | 4 (5) | -4 (-4) | -4 | 10 | -0.3 | 1 |

**Table 6:** The radiative and turbulent fluxes averaged over the hot subtropical desert domain during JJAS season for the positive albedo perturbation experiments. Asterisk ($^*$) in Table indicates that the flux values are averaged only over 15°-40°N and 35°-75°E (e.g. in the Desert_Arab_p20 experiment). Fluxes are signed in the direction of the fluxes (i.e. negative sign indicates upward fluxes and vice-versa). The upper part of the Table provides the climatological estimates from the sensitivity experiments while the lower part shows the anomalous responses (deviations from the CTRL climatology). All fluxes have energy units ($Wm^{-2}$) and albedo is in %, while TS and PR have the units of K and mm $day^{-1}$, respectively.

| | Albedo at TOA (SURF) | Net SW at TOA (SURF) | LWat TOA (SURF) | Net LW at TOA (SURF) | Net Rad at TOA (SURF) | LH Flux | SH flux | TS | PR |
|---|---|---|---|---|---|---|---|---|---|
| | | Climatological responses | | | | | | | |
| Desert_p20 | 37 (51) | 283 (156) | -293 (-454) | -293 (-110) | -10 (46) | -7 | -35 | 298.8 | 0.1 |
| $^*$Desert_Arab_p20 | 35 (46) | 289 (171) | -299 (-460) | -299 (-111) | -9 (60) | -11 | -44 | 299.7 | 0.2 |
| | | Anomalous responses | | | | | | | |
| Desert_p20 | 9 (21) | -40 (-46) | 1 (43) | 1 (6) | -39 (-40) | 2 | 38 | -6.8 | -0.2 |
| $^*$Desert_Arab_p20 | 9 (2) | -42 (-48) | 4 (32) | 4 (8) | -37 (-40) | 3 | 38 | -5 | -0.15 |

**Table 7:** The radiative and turbulent fluxes averaged over Indian landmass (land points only: 75°-90°E, 5°-25°N) during JJAS season for the positive albedo perturbation experiments. Fluxes are signed in the direction of the fluxes (i.e. negative sign indicates upward fluxes and vice-versa). The upper part of the Table provides the climatological estimates from the sensitivity experiments while the lower part shows the anomalous responses (deviations from the CTRL climatology, see Section 2). All fluxes have energy units ($Wm^{-2}$) and albedo is in %, while TS and PR have the units of K and mm $day^{-1}$, respectively.

| | Albedo at TOA (SURF) | Net SW at TOA (SURF) | LWat TOA (SURF) | Net LW at TOA (SURF) | Net Rad at TOA (SURF) | LH Flux | SH flux | TS | PR |
|---|---|---|---|---|---|---|---|---|---|
| | | Climatological responses | | | | | | | |
| Desert_p20 | 31 (16) | 306 (199) | -251 (-487) | -251 (-70) | 55 (129) | -44 | -85 | 304.3 | 2.8 |
| Desert_Arab_p20 | 34 (16) | 294 (184) | -241 (-483) | -241 (-59) | 53 (125) | -53 | -72 | 303.6 | 3.8 |
| | | Anomalous responses | | | | | | | |
| Desert_p20 | -8 (0) | 37 (45) | -28 (-13) | -28 (-29) | 9 (16) | 24 | -38 | 2 | -3.2 |
| Desert_Arab_p20 | -5 (0) | 25 (30) | -18 (-9) | -18 (-18) | 7 (12) | 15 | -25 | 1.3 | -2.2 |